CHAPTER I

INTRODUCTION

1.1 Background and motivation

The development of advanced materials has greatly influenced modern technology. Metal oxide thin films, especially bismuth ferrite ($BiFeO_3$ or BFO), have gained a lot of interest because of their unique properties and potential uses in electronic and spintronic devices. BFO is a multiferroic material, which means it shows more than one ferroic order parameter, like ferroelectricity and antiferromagnetism. This rare mix of properties makes BFO a great choice for advanced multifunctional devices, as it can control magnetic states with electric fields and vice versa (Achenbach et al., 2006; Michel et al., 1969; Smolenskii, 1959). The properties of BFO thin films are well known. A key finding was the significant ferroelectric polarization of about 60 $\mu C/cm^2$ in BFO epitaxial thin films grown on $SrRuO_3$ (SRO)/$SrTiO_3$ (STO) substrates, which is about 15 times higher than that of bulk BFO This finding opened new opportunities for using BFO in memory devices and spintronic applications, showing its potential in quantum effects and nanoscale device fabrication. As materials are reduced to the nanoscale, quantum effects become more noticeable, leading to unique and useful physical phenomena (Connerade, 2009). Controlling the size and shape of nanostructures is important for using these quantum effects. Advanced nanomanufacturing techniques, such as focused ion beam (FIB) and electron beam lithography (EBL), help create precise nanostructures needed for devices that use quantum mechanical properties (Hong et al., 2009; Kim et al., 2018).

This research aims to explore and use the unique properties of BFO thin films at the nanoscale. By understanding and manipulating these properties, we hope to improve the performance and function of electronic devices. The research aims to connect basic material science with practical applications, leading to more efficient, reliable, and multifunctional next-generation technologies. Besides the scientific and

technological reasons, there is a practical need to develop good methods for making and studying these nanostructures. Techniques like FIB and EBL are not only important for creating precise nanostructures but also for studying how size, shape, and material properties interact at the nanoscale. By improving these techniques and understanding their impact on material properties, we can better control the functionality of the devices. Additionally, integrating nanostructures into devices requires understanding their electrical and mechanical properties. For instance, the piezoelectric and ferroelectric properties of BFO thin films can be greatly affected by factors like crystallinity, grain size, and domain structure. Techniques such as Piezoresponse Force Microscopy (PFM) offer valuable insights into these properties, allowing for detailed characterization and optimization of nanostructures (Kalinin et al., 2002).

In this work, this research focuses on exploring quantum effects in metal oxide thin films, particularly BFO, at the nanoscale and developing advanced nanomanufacturing techniques to control the size and shape of these nanostructures. This work aims to improve the performance and function of future electronic devices, contributing to technological advancement in various fields. We studied the ferroelectric property of BFO with different substrate Nb-doped $SrTiO_3$ (NSTO) and Fluorine-doped Tin Oxide (FTO) glass. Together with, the different shape in nanoscale, generating the pattern by the nanomanufacturing such as FIB and EBL was investigated. The ferroelectric response of Annealed BFO/NSTO in unpattern and pattern areas and Au Nanohole array were demonstrated. Moreover, we explored the piezoresponse of the BFO/NSTO sample under UV irradiation. So, this polarization can be controlled the by UV exposure. These results are crucial for understanding how UV light influences ferroelectric properties and for creating applications in optoelectronic devices that use controlled UV exposure.

1.2 Research objectives

1) To use nanomanufacturing techniques for precision control over the size and shape of BFO nanostructures.

2) To investigate the impact of nanoscale patterning on the ferroelectric properties of BFO thin films

3) To investigate the properties of Bismuth Ferrite (BFO) thin films under light irradiation.

1.3 Outline of thesis

To help you understand the overview of this dissertation, each chapter is described below. The thesis is divided into five main chapters. Chapter I provides an introduction, outlining the background, motivation, research objectives, and the thesis structure. Chapter II offers a comprehensive literature review, discussing the structure, production, and properties of BFO thin films, along with nanopatterning methods and their effects. It also covers the dynamic and non-dynamic mechanisms affecting the films under light irradiation. Chapter III details the methodology, including substrate preparation, sample fabrication, and the equipment used, focusing on metal oxide thin films and nanoscale patterning techniques. Chapter IV presents the results and discussion, examining the crystal structure, surface morphology, and ferroelectric properties of BFO/NSTO and Au nanohole array on BFO/FTO. Finally, Chapter V concludes the thesis, summarizing the key findings and suggesting directions for future research.

CHAPTER II

LITERATURE REVIEWS

This chapter will primarily introduce the knowledge related to $BiFeO_3$ (BFO) thin films, including their structure, production, and properties. It will also review the nanopatterning method and its effects on BFO Thin film. There are two main mechanisms that explain the effect of light irradiation on the surface of the sample. Firstly, dynamic mechanism includes the photoelectric photoconductivity, and ferroelectric photovoltaic effects. While two-dimensional electron gases and oxygen vacancy are categorized as a non-dynamic mechanism.

2.1 Bismuth Ferrite ($BiFeO_3$)

The study of BFO was initiated by Smolenskii in 1959, revealing its potential as a multiferroic material. However, due to the difficulty in growing single-phase BFO, it did not attract much interest from researchers at the time (Smolenskii, 1959). By the late 1960s, researchers proposed a solution to this problem by treating BFO with HNO_3 (nitric acid) to eliminate secondary phases. This approach successfully synthesized single-phase BFO (Achenbach et al., 2006; Michel et al., 1969). A significant milestone occurred a few decades later when Kubel and Schmid discovered the monodomain single-phase BFO in 1990 using X-ray diffraction measurement, which revealed its intrinsic properties (Kubel et al., 1990). In 2003, Another milestone was set when Wang et al. demonstrated a significant ferroelectric polarization of approximately 60 $\mu C/cm^2$ in BFO epitaxial thin films grown on an SRO/STO substrate, which is about 15 times higher than that of bulk BFO (Wang et al., 2003). This marked the first instance of achieving such high polarization in BFO thin films, opening new opportunities for use in memory devices and next-generation spintronic devices.

At room temperature, the single-phase structure of BFO is described as a rhombohedral distorted perovskite, categorized under the R3c space group (Moreau et al., 1971). Figure 2.1 shows the structure of perovskite BFO, where the Bi ion is located at the corners, the Fe ion at the center, and 6 oxygen ions at the face centers (Hiroshi, 2011). BFO exhibits ferroelectric properties below its Curie temperature ($T_C \approx 1103$ K) and antiferromagnetic properties below its Néel temperature ($T_N \approx 643$ K) in ceramic bulk form (Sosnowska et al., 1982). The rhombohedral structure of perovskite BFO has lattice parameters of a = 3.96 Å and a rhombohedral angle of α = 89.4° at room temperature. It exhibits ferroelectric polarization along the pseudocubic [111] direction .

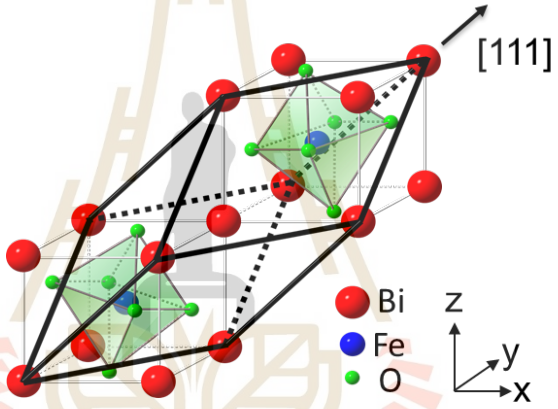

Figure 2.1 A diagram showing the rhombohedral structure of perovskite BFO, which belongs to the R3c space group, with two unit cells aligned along the [111] direction. (Hiroshi, 2011).

2.1.1 Bismuth ferrite thin films preparation

BFO thin films can be prepared using various thin film deposition methods. These methods include metal organic chemical vapor deposition (MOCVD), electron beam (e-beam) evaporation, pulsed-laser deposition (PLD), spray pyrolysis, chemical solution deposition (CSD), the sol-gel method, and radio frequency (RF) magnetron sputtering. Each method has its own set of trade-offs between cost, complexity, film quality, and suitability for different applications. Hence, the choice of method depends on the specific requirements of the BFO thin films. For instance, MOCVD and spray pyrolysis are generally employed to grow films at high temperatures, around 800 °C (Micard et al., 2020). As a result, these techniques are unsuitable for

producing BFO thin films intended for low operating temperatures. While PLD and e-beam evaporation are limited to growing films on small substrate areas. Consequently, these techniques are unsuitable for producing large-scale homogeneous thin films (Mijiti et al., 2021; Pei et al., 2020; You et al., 2018; Zhang et al., 2018). CSD and sol-gel methods apply thin films to substrates at ambient temperature. However, these films require high post-annealing temperatures, around 700 °C, for crystallization (Yang et al., 2021). As a result, RF magnetron sputtering is often chosen for growing high-quality thin films on large area substrates at low temperatures. This method is straightforward, easy to scale up, and highly compatible with electronic industry needs (Li et al., 2008; Wu et al., 2010; Zhu et al., 2018).

The RF magnetron sputtering method uses alternating current (AC) to avoid charge buildup on the oxide sputtering target. The process begins by evacuating the sputtering chamber to reach a high vacuum level of 10^{-7} Torr. Next, an inert gas like argon is introduced into the chamber, increasing the pressure to 10^{-3} Torr. A RF voltage is applied between the substrate (anode) and the target (cathode). As the power supply gradually increased, the argon gas ionizes into Ar^{+} ions and electrons. The Ar^{+} ions gain energy corresponding to the voltage between the substrate and the target, accelerating due to the electric field from the applied voltage and bombarding the target surface. Atoms are sputtered off the target, becoming vapor and then depositing on the substrate. Meanwhile, the ionized electrons are trapped near the target by magnets placed behind the cathode, enhancing the bombardment process. (Feng, 2018). Figure 2.2 illustrates a schematic diagram of the fundamental components of a magnetron sputtering system.

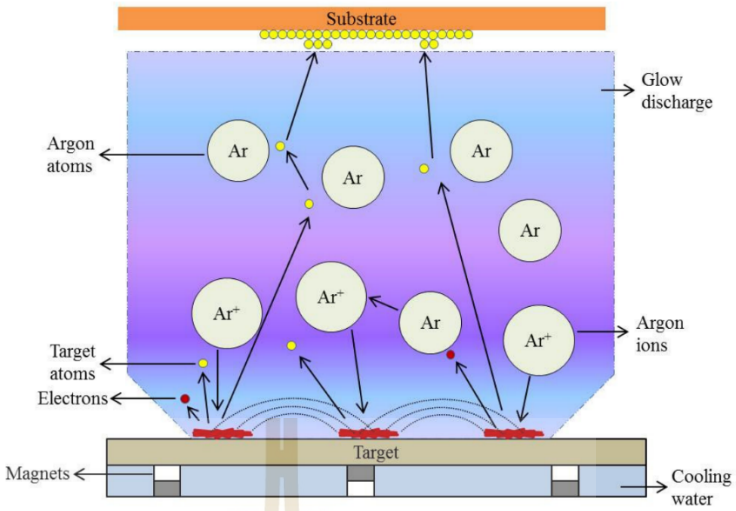

Figure 2.2 The schematic diagram of the fundamental components of a magnetron sputtering system (Maurya et al., 2014).

2.1.2 Ferroelectric property in Bismuth ferrite thin films

Ferroelectric materials exhibit spontaneous electric polarization, which can be switched by applying an electric field (Lines et al., 2001). In perovskite oxide materials, the ferroelectric phase occurs when they transition from a centrosymmetric cubic phase at high temperatures to a lower symmetry phase below the transition temperature, known as the Curie temperature. This mechanism occurs when cations move relative to the anions in the oxide perovskite, creating an electric dipole moment that results in spontaneous polarization. At room temperature, ceramic bulk BFO exhibits both ferroelectric and antiferromagnetic properties because of its high Curie temperature ($T_C \approx 1103$ K) and Néel temperature ($T_N \approx 643$ K) (Sosnowska et al., 1982). In 2003, researchers observed a significant remanent polarization of around 60 μC/cm² in 200-nm-thick epitaxial BFO thin films grown on an SRO/STO (001) substrate for the first time, as depicted in Figure 2.3(a) (Wang et al., 2003). These thin films showed a spontaneous polarization at room temperature that was higher than the bulk BFO, which is approximately 6.1 μC/cm² (Teague et al., 1970).

Approximately a year later, researchers investigated how substrate orientation affects ferroelectric properties. They grew pure phase of BFO thin films with thickness 200 nm on (111), (101), and (001) SRO/STO substrates. The hysteresis loops for these orientations showed remanent polarization (P_r) values of around 100, 80, and 55 μC/cm² for (111), (101), and (001) STO substrates, respectively. A single crystal with a rhombohedral structure of BFO films grown on the (111) orientation was exhibited, while those on the (101) or (001) orientations were monoclinically distorted from the rhombohedral structure due to the epitaxial constraint (Li et al., 2004). Similarly, Das et al. also prepared 600-nm-thick BFO thin films on STO substrates with (001), (101), and (111) orientations. The resulting hysteresis loops showed remanent polarization (Pr) values of approximately 98, 86, and 55 μC/cm² for (111), (101), and (001) STO substrates, respectively, as illustrated in Figure 2.3(b) (Das et al., 2006). Both studies suggest that the direction of spontaneous polarization is nearly aligned with the (111) orientation, similar to that observed in bulk crystals and ceramics.

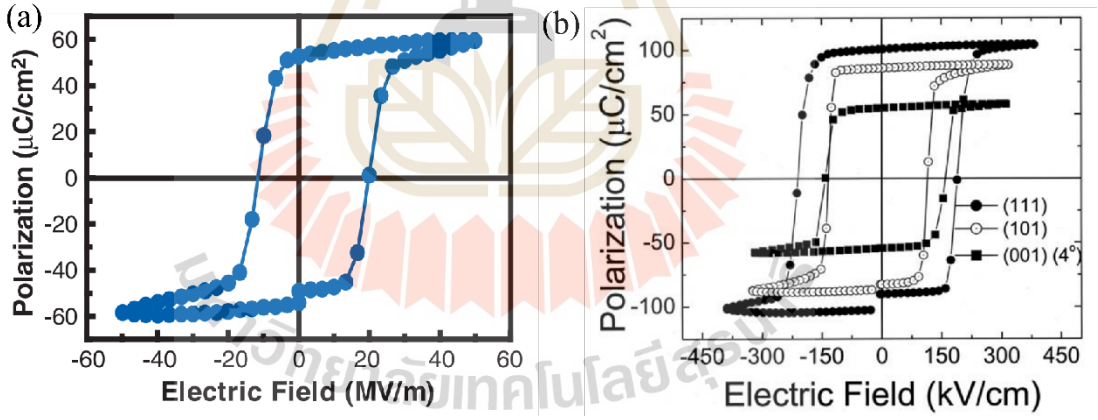

Figure 2.3 The hysteresis loop of BFO/SRO/STO sample (a) at 15 kHz (Wang et al., 2003) and (b) at orientation of (111), (101), and (001) BFO films (Das et al., 2006).

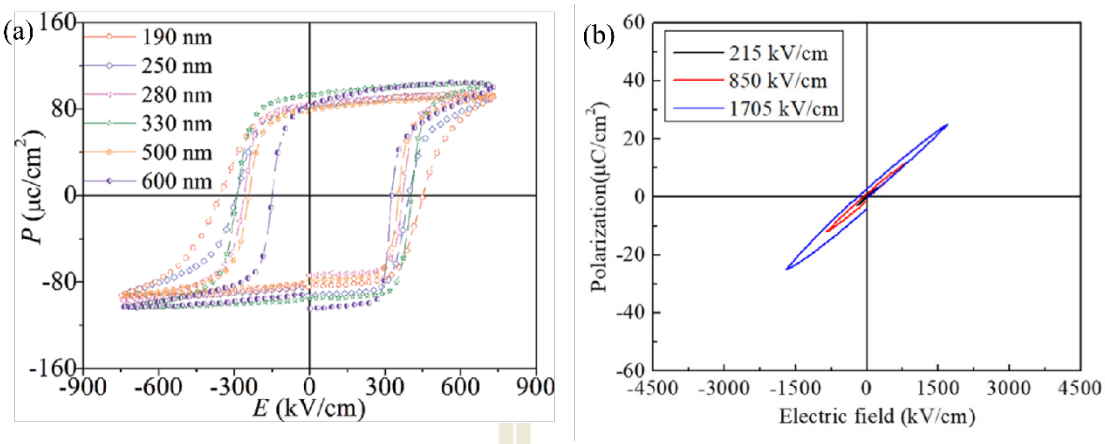

Figure 2.4 The hysteresis loop (a) BFO thin films different thicknesses of 190-600 nm on SRO/Pt/TiO_2/SiO_2/Si substrate at 1 kHz (Wu et al., 2011) and (b) various electric fields of amorphous BFO thin films on Pt/Ti/SiO_2/Si substrate (Li et al., 2021).

Pure phase BFO thin films with varying thicknesses from 190 to 600 nm were grown on SRO/Pt/TiO_2/SiO_2/Si (100) substrates using RF sputtering. At 1 kHz and room temperature, these films exhibited significant polarization, ranging from about 80 to 95 μC/cm², with a mixture of (110) and (111) orientations, as shown in Figure 2.4(a) (Wu et al., 2011). The highest spontaneous polarization is observed in the (111) direction for BFO thin films because ions are displaced along the pseudocubic [111] direction from their equilibrium positions (Ederer et al., 2005). Consequently, the combination of both orientations greatly improves the ferroelectric properties of BFO thin films.

2.1.3 Nanolithography on Bismuth ferrite thin films

Nanolithography techniques have emerged as vital tools in this field, enabling the creation of nanostructures with precise control over their size and properties. Among these techniques, Dip-Pen Nanolithography (DPN), Electron Beam Lithography (EBL), and Focused Ion Beam (FIB) milling have been extensively explored for fabricating BFO nanostructures. Each method offers unique advantages and limitations, which can significantly impact their suitability for specific applications.

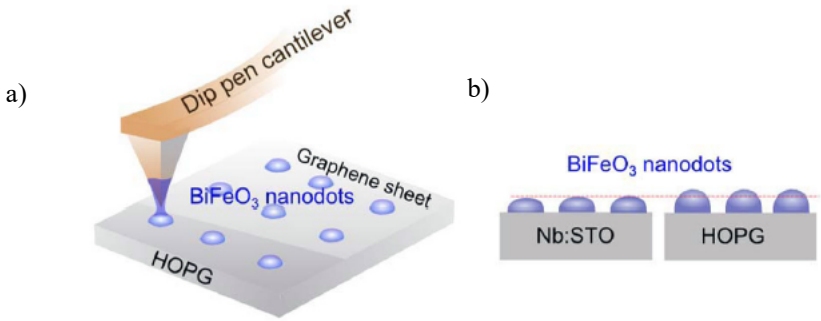

Figure 2.5 Schematic diagrams showing the DPN of BFO nanodots: (a) a nano-pattern using a BFO precursor sol by DPN, (b) BFO nanodots prepared on Nb-STO and HOPG substrates (Kim et al., 2013).

Dip-Pen Nanolithography (DPN) uses an atomic force microscope (AFM) tip to precisely deposit materials onto a surface. The AFM tip, typically made of silicon, is dipped into an "ink" solution containing the material to be deposited. When the tip touches the surface, a small liquid bridge forms, allowing the material to transfer and create patterns. The movement of the AFM tip is carefully controlled, allowing for the creation of very small and precise structures. After the material is deposited, the surface is often heated to improve its properties. DPN can use various materials and is useful for making tiny electronic components and sensors. This method doesn't require additional steps like masks, making it a simple and effective way to create nanoscale patterns (Jung et al., 2012).

EBL is a high-resolution nano-patterning method that employs a focused beam of electrons to produce accurate patterns on a substrate (Tseng et al., 2003). The process begins with coating the substrate with an electron-sensitive resist, typically a polymer like polymethyl methacrylate (PMMA) (Shahali et al., 2019). The substrate is then exposed to a focused electron beam that scans the surface according to a computer-aided design (CAD) file. This exposure changes the chemical structure of the resist in the scanned areas. The substrate is then developed, dissolving the exposed areas of the resist in positive resists or the unexposed areas in negative resists. The remaining resist pattern acts as a mask for subsequent etching or material

deposition steps. Finally, the remaining resist is then removed, leaving the desired pattern on the substrate (Chen, 2015).

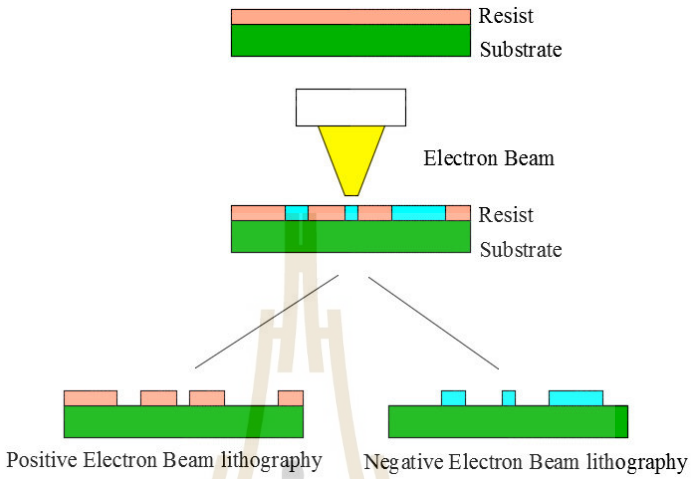

Figure 2.6 The Principal of EBL (Shahali et al., 2019).

FIB milling is a high-resolution fabrication technique (10-30 nm) used for imaging and fabricating various materials, such as silicon wafers, polymers, and metals. The FIB principle is similar to that of Scanning Electron Microscopy (SEM), but instead of electrons, it uses ions like Ga^+, Ne^+, or He^+ (Rodriguez Hernandez et al., 2015). As shown in Figure 2.7, the interaction volumes of gallium ions, electrons, and helium ions differ. The interaction volume for secondary electrons (SE) produced by a focused He+ beam is much smaller than that produced by electrons or Ga^+, meaning that a Helium Ion Microscope (HIM) provides better resolution for imaging compared to Ga^+-FIB and SEM. Conversely, Ga^+ ions have a high mass, causing significant surface scattering. HIM can also scatter the surface at 30 keV, and because He^+ ions have a low mass, it is advantageous for fabricating very small features at the sub-nanometer scale (Hlawacek et al., 2014).

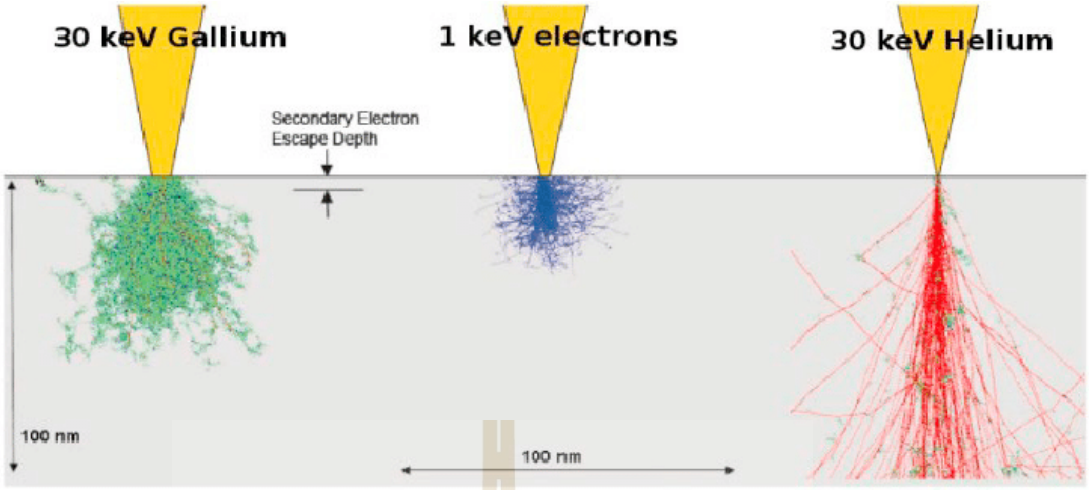

Figure 2.7 Differences in interaction volumes among various charged particle beams used for imaging (Hlawacek et al., 2014).

In 2006, Tao Sun and colleagues reported the fabrication of BFO nanopatterns using soft electron beam lithography, which combines electron beam lithography with the spinning of sol-gel precursors on an STO substrate (Sun et al., 2006). Firstly, a polymer and PMMA were sequentially spun onto the substrates as electron beam resist. The electron beam was then used to pattern arrays of disks or lines on the resist. BFO sol was spun onto the substrate and dried at 150°C to gel the sol after developing. The samples were then immersed in acetone to remove the electron beam resist and remove excess BFO from the unpatterned areas. Finally, crystalline BFO patterns were obtained by annealing the samples at 600°C for 30 minutes. The BFO nanolines with 80 nm of linewidth patterned on STO substrate exhibit an bamboolike microstructure that could be useful for studying the role of grain boundaries in influencing the leakage current in BFO (Sun et al., 2006).

In 2012, Inhwa Jung and colleagues used Dip-Pen Nanolithography (DPN) with a silicon nitride cantilever to create BFO nanodots on a NSTO substrate. The size of the BFO nanodots ranged from 30 to 180 nm, depending on the deposition time, which varied between 0.1 and 10 seconds. The array of BFO nanodots was well-formed, with a minimum gap of around 30 nm between the dots (Jung et al., 2012). Notably, the minimum-sized BFO nanodot is characterized to be a single domain with the lateral dimension of 30 nm and thickness of 16 nm. It also showed a good

ferroelectric switching characteristics with only 1V bias potential. One year later, Woo-Hee-kim and colleagues investigated the comparative BFO nanodot study between NSTO and highly ordered pyrolytic graphite (HOPG) substates using Dip-Pen Nanolithography (DPN). The result suggested that BFO nanodot on the HOPG substrate is smaller in lateral size and higher in thickness compared to NSTO substrate. Additionally, PFM measurements showed that BFO nanodots on HOPG have better ferroelectric properties compared to those on NSTO, with a ratio of 1.2:1. This is due to the reduced substrate clamping effect and improved piezoresponse properties (Kim et al., 2013).

In 2009, Seungbum Hong and co-workers fabricated epitaxial BFO nanostructures with three layers BFO, SRO and STO respectively from top to bottom. The BFO layer was patterned into the square shape of 500x500 nm^2 in size and round shape of 500 nm in diameter by using focused Ion beam (FIB) lithography. They reported the ferroelectric domain configuration and switching behavior depend on the shapes. Square-shaped nanostructures show a single variant domain, whereas round-shaped nanostructures display seven variants of domain configuration. They also found that the round-shaped nanostructures provide more symmetric hysteresis loops (Hong et al., 2009). In 2018, Bumsoo Kim and colleagues used angle-resolved piezorespose force microscope (AR-PFM) to investigated ferroelectric domain in BFO/SRO/STO substrate patterned by combined EBL and FIB techniques. They found that the removal of the film surrounding the structures from patterning caused elastic relaxation, leading to a reduction in the average number of neighboring domains. This indicates a decrease in domain complexity. Additionally, the result also revealed that the higher aspect ratio patterning structures provides a simpler domain configuration and better piezoresponse characteristics, such as lower coercive voltage and higher remanent piezoresponse (Kim et al., 2018) as illustrated in Figure 2.8.

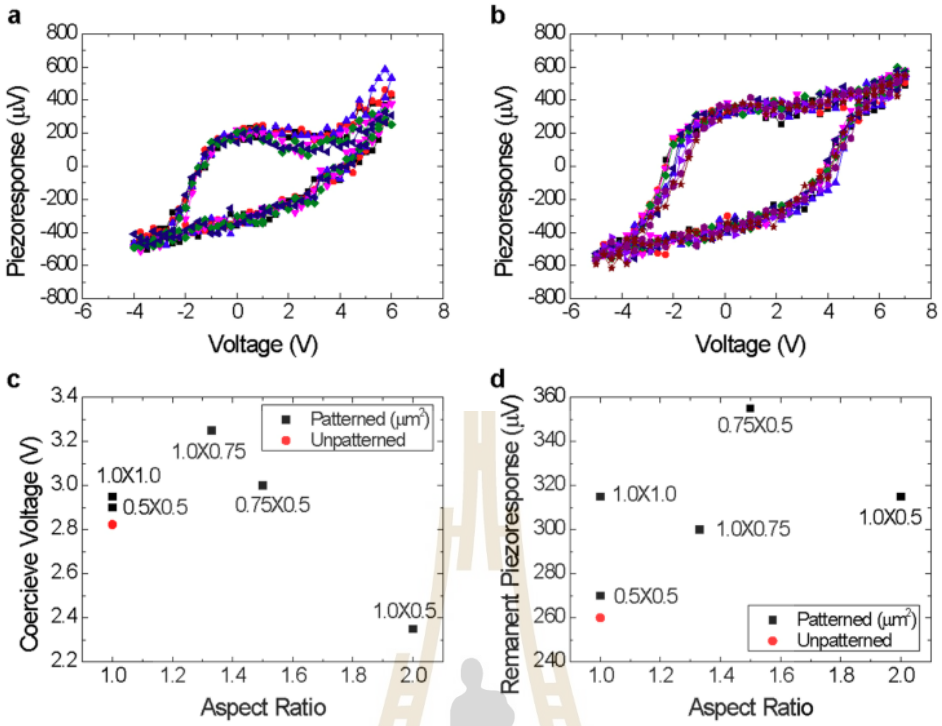

Figure 2.8 Piezoresponse measurement for (a) unpatterned BFO film and (b) 0.75 μm×0.5 μm patterned BFO structure. (c) Coercive voltage and (d) remanent piezoresponse of the patterned BFO structures and the unpatterned BFO film (Kim et al., 2018).

2.2 Dynamic mechanism

2.2.1 Photoelectric effect

The photoelectric effect is a phenomenon in which electrons are emitted from a material's surface upon absorbing electromagnetic radiation, a process also known as photoemission. The emitted electrons are termed photoelectrons. Discovered by Heinrich Hertz in 1887, the photoelectric effect was observed when ultraviolet light shone on two metal electrodes with a voltage applied across them, causing a change in the voltage between the electrodes. This phenomenon, which classical physics could not explain, demonstrated the interaction between light and matter and characterized light as an electromagnetic wave. In 1905, Einstein explained through quantum mechanics that each particle of light, called a photon, carries a fixed amount of energy, given by ($\mathbf{E = h\nu}$), where $\boldsymbol{\nu}$ is the light's frequency and $\mathbf{h}$ is Planck's

constant. The work function (w) is a metal's intrinsic property, representing the minimum energy required to remove an electron from the metal's surface. When the energy of a photon exceeds the work function, the kinetic energy ($\mathbf{E_k}$) of the ejected electron can be expressed as shown in equation (2.1).

$$\mathbf{E_k = h\nu - w} \tag{2.1}$$

Where $\mathbf{E_k}$ is the kinetic energy of the ejected electron, h**ν** is the energy of the incident photon. When an electron is ejected, the incident photon's energy (h**ν**) must overcome both the binding energy ($\mathbf{E_b}$) and work function (**w**). Therefore, we can write in (2.2).

$$\mathbf{h\nu = E_b + w + E_k} \tag{2.2}$$

The kinetic energy of the ejected electron can be written as in equation (2.3).

$$\mathbf{E_k = h\nu - E_b - w} \tag{2.3}$$

From this equation, the binding energy can be represented as shown in equation (2.4).

$$\mathbf{E_b = h\nu - E_k - w} \tag{2.4}$$

2.2.2 Ferroelectric photovoltaic effect

Ferroelectric materials have the ability to exhibit spontaneous polarization, which can be switched by applying an external electric field (Lines et al., 2001). When light interacts with ferroelectric materials, it generates pairs of electrons and holes, leading to a steady-state photocurrent, a phenomenon known as the photovoltaic effect. Ferroelectric photovoltaic (FEPV) effects occur in these materials, producing photovoltage and photocurrent along the polarization direction. FEPV effects differ from conventional photovoltaic devices in two key aspects. Firstly, in typical photovoltaic devices, electron-hole pairs in a semiconductor material are generated by light absorption. Electron-hole pairs are separated by an electric field within a micrometer-thick depletion region, with the maximum voltage produced being equivalent to the semiconductor band gap ($\mathbf{E_g}$). In contrast, ferroelectric materials achieve charge separation through spontaneous electric polarization, resulting in a

photovoltage significantly greater than the band gap, known as the anomalous photovoltaic effect (Yang et al.). Secondly, in ferroelectric materials, the direction of photovoltage and photocurrent can be reversed by altering the polarization direction. (Choi et al., 2009). Consequently, ferroelectric materials have the potential to achieve better power conversion efficiency (PCE) compared to conventional photovoltaic materials, offering exciting possibilities for the future of solar energy and related technologies. A schematic representation of FEPV devices, including lateral and vertical structures, is shown in Figure 2.9 (Yuan et al., 2014). These devices feature two electrodes, a cathode and an anode.

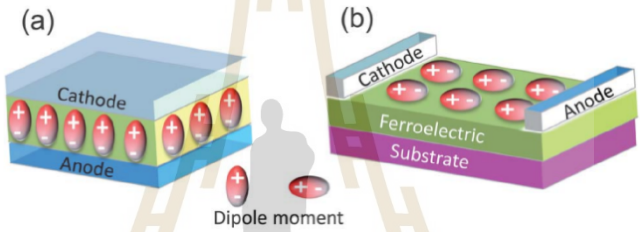

Figure 2.9 The schematic diagram illustrates the ferroelectric photovoltaic device, (a) vertical and (b) lateral configurations. (Yuan et al., 2014).

The polarization direction in ferroelectric materials is indicated by the electric dipole moment. Several factors influence the photovoltage, such as the electrodes, light intensity, remnant polarization in the ferroelectric materials, the distance between, domain walls, crystal orientation, and the interface of the ferroelectric-metal. Various mechanisms have been suggested to explain the superior voltage output of FEPV materials.

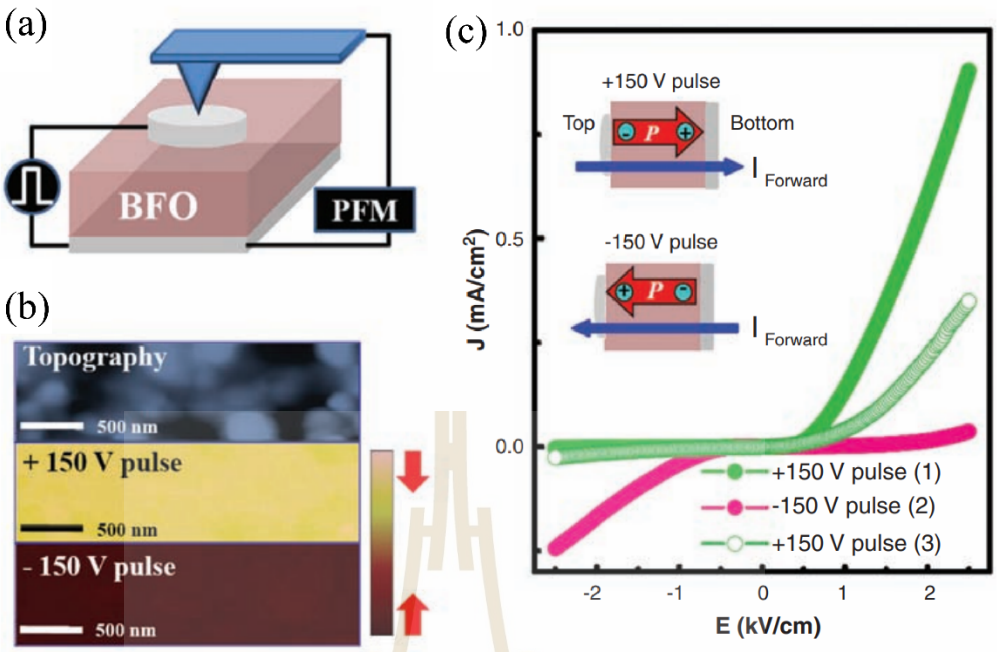

Figure 2.10 (a) The schematic setup for PFM and current density J(E) measurements on Ag/BFO/Ag samples subjected to electric pulses of ±150 V (with an electric field E≈17 kV/cm). (b) The top panel shows the topography, and the middle and bottom panels display out-of-plane PFM images color-scaled after applying +150 V and -150 V pulses, respectively. (c) The J(E) curves after applying different voltage pulses: +150 V, -150 V, and +150 V, respectively (Choi et al., 2009).

Choi et al. reported a diode effect in the BFO crystal characterized by nonlinear, unidirectional, and high electric conduction. This effect is associated with the direction of electric polarization in the bulk material. When an external electric field switches the electric polarization, the diode effect also reverses. The system consists of a thin, platelike BFO crystal with a thickness of approximately 90 μm and in-plane dimensions of about 1×2 mm², along with a circular Ag electrode of around 0.6 mm thickness, as illustrated in Figure 2.10(a). The forward and reverse bias directions are altered by applying high electric voltage pulses.

When the Ag/BFO/Ag samples are subjected to electric pulses of +150 V (with an electric field strength of approximately $\mathbf{E} \approx 17$ kV cm^{-1}) on the top electrode, the polarization direction points downward. This is evident in the Piezoresponse Force Microscopy (PFM) image displayed in Figure 2.10(b). The electric current flows downward direction through the sample, causing the diode to have a forward direction from top to bottom, as depicted in the $\mathbf{J(E)}$ curve in Figure 2.10(c) (Choi et al., 2009).

In contrast, applying -150 V electric pulses to the top electrode reversed the ferroelectric polarization orientation to the upward direction. Consequently, the diode's forward direction shifted from bottom to top, following the polarization axis, now referred to as the reverse bias direction. This is depicted by the pink line in Figure 2.10(c). After applying both +150 V and -150 V pulses, a second round of +150 V pulses was administered. However, this second application of +150 V pulses did not fully restore the original $\mathbf{J(E)}$ curve. This could be due to various factors, such as partial polarization reversal or the formation of conducting pathways (Choi et al., 2009).

2.3 Non-dynamic mechanism

2.3.1 Electronic structures of two-dimensional electron gases

A two-dimensional electron gas (2DEG) is a layer where electrons are free to move in two dimensions. At the interface of semiconductor heterostructures, such as the $LaAlO_3$ (LAO)/$SrTiO_3$ (STO) junction, a 2DEG forms due to the differing electronic properties of the materials. This confinement leads to distinctive electronic properties like high electron mobility and quantum effects (Ohtomo et al., 2004). The formation and control of a 2DEG on the bare STO surface under ultraviolet (UV) light exposure. Using angle-resolved photoemission spectroscopy (ARPES), the researchers investigate 2DEG states on lightly La-doped STO samples. The study finds that a notable 2DEG can form on the bare STO surface, akin to the one observed at the LAO/STO interface (Meevasana et al.). It shows that the 2DEG density can be controlled by adjusting the UV irradiation dose. The experiments indicate that the 2DEG on STO is likely due to oxygen vacancies created during UV exposure, rather than a polar

interface. The results offer a deeper understanding of 2DEG formation mechanisms and suggest new possibilities for oxide electronics development. The 2DEG states on the STO surface and the related momentum distribution curves are shown in Figure 2.11(a) and (b). Figure 2.11(c) displays the Fermi surface map representing the total surface charge density, consistent with 2DEG densities measured at LAO/STO interfaces (Kalabukhov et al., 2007). Figure 2.11(d) depicts the schematic Fermi surface and band dispersions derived from the measured electronic structure. These results demonstrate that a 2DEG can be generated on the UV-irradiated STO surface (Meevasana et al., 2011).

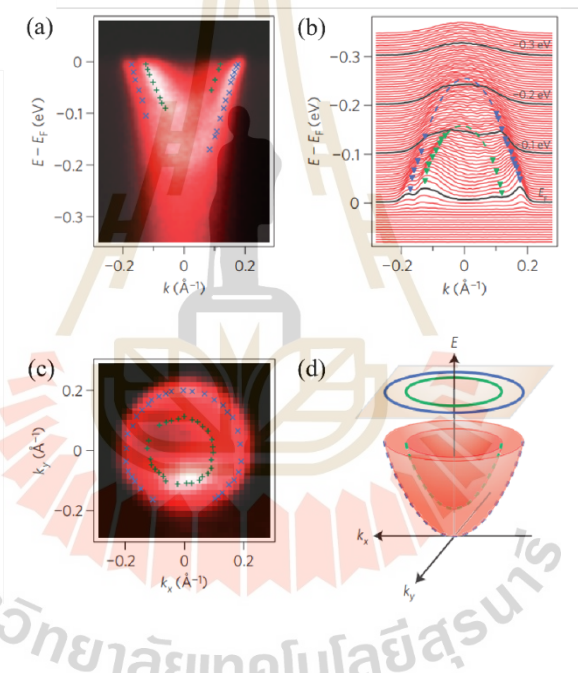

Figure 2.11 The 2DEG states of La-doped STO after UV light exposure. (a) ARPES data of La-doped STO at T = 20 K, (b) Corresponding momentum distribution curves with parabolic fits to the data points. (c) Fermi surface map. (d) Schematic Fermi surface and band dispersions obtained from the electronic structure measurement. (Meevasana et al., 2011).

Recently, the 2DEG has been studied in perovskite heterostructures, specifically at the BFO and STO interfaces. Theoretical calculations indicate that the 2DEG forms at the $(BiO)^{+}$ and $(TiO_2)^{0}$ interfaces (Zhang et al., 2011). From a chemical standpoint, the BFO/STO heterostructure exhibits similar characteristics to the

LAO/STO heterostructure. However, BFO demonstrated both ferroelectric and magnetic characteristics at room temperature (Catalan et al., 2009; Ederer et al., 2005; Lebeugle et al., 2007), a distinction that LAO lacks. The BFO/STO structure is distinct from the LAO/STO structure in its formation of a metallic character due to a 2DEG state. Conductive atomic force microscopy (C-AFM) was used to examine a 20 μm-thick cross-sectional sample of the BFO/STO interface. Figure 2.12 shows the surface topographic imaging and nanoscale current mapping of this interface. The results indicated a significantly higher current at the interface compared to the bulk materials, suggesting the formation of a 2DEG due to its conductive nature. According to (Chen et al., 2015), this phenomenon is attributed to the variation in valence state caused by the diffusion of Ti from STO into the Fe sites of BFO at the interface.

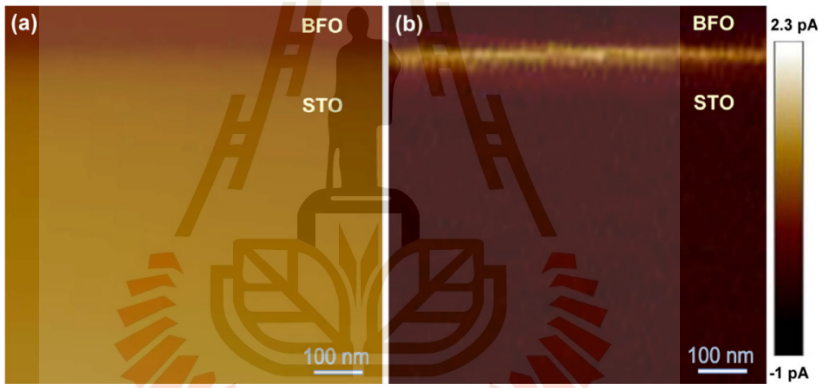

Figure 2.12 The presence of a 2DEG at the interface between BFO and STO is demonstrated using (a) a surface topography image and (b) nanoscale current tracing (Chen et al., 2015).

The conducting interface can be controlled by the ferroelectric polarization of a BFO/STO superlattice (Fu et al., 2021) and a BFO/$TbScO_3$ (TSO) heterostructure (Zhang et al., 2018) Under UV irradiation, the formation of a 2DEG state induced by oxygen vacancies has been reported in the slightly doped metal $Bi_{0.95}La_{0.05}FeO_3$ (BLFO) (Nathabumroong et al., 2020). So far, creating a 2DEG has required epitaxially grown BFO thin films. To achieve this, BFO thin films need to be grown on STO (100) substrates at high temperatures (580-750 °C) (Ji et al., 2010; Nakashima et al., 2015; Nakashima et al., 2020; Saenrang et al., 2017). However, there

are a few studies on amorphous oxides on STO substrates that can also create a 2DEG through the formation of oxygen vacancies (Lee et al., 2012; Li et al., 2018; Scigaj et al., 2015).

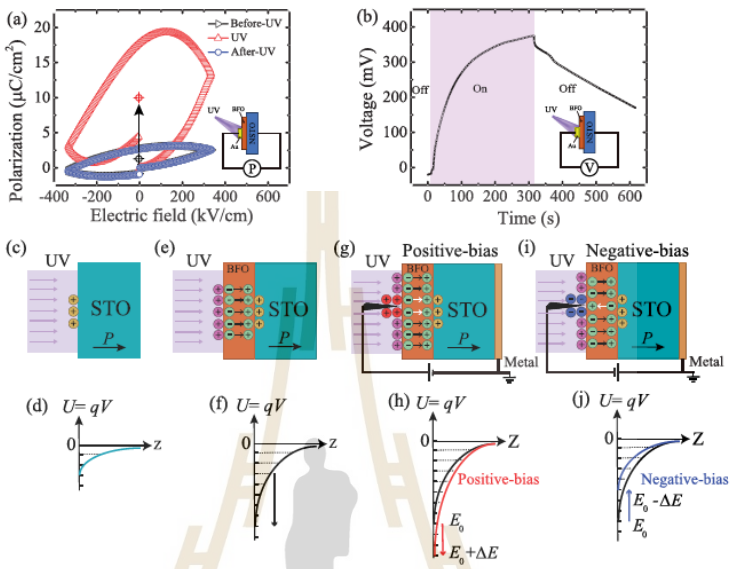

Figure 2.13 Mechanisms of 2DEG formation and modulation in amorphous BFO/NSTO thin films Interface (a) the polarization-electric field (P-E) hysteresis loops of under UV illumination. This indicates the electrical polarization behavior which contributes to the formation of the 2DEG. (b) Illustrates the time-dependent voltage with UV irradiation cycles. This voltage difference is related to the induced electric field and polarization, crucial for understanding the modulation of 2DEG. (c)–(j): Provide schematic diagrams of UV-light-induced oxygen vacancies and the resultant quantum well states (Laohana et al., 2022).

In 2022, Peerawat Laohana and co-workers studied the photo-induced conductivity of a 2DEG at the interface of STO and BFO. The BFO is deposited using radio frequency magnetron sputtering. The findings show a significant increase in photo-induced conductance at the BFO/STO interface, up to 20.62 times higher than the sum of individual BFO and STO conductance. This enhancement is attributed to the strong photo-induced electrical polarization of BFO, which can be modulated by an electric field, exhibiting diode-like behavior. In figure 2.13 demonstrates the mechanisms behind the formation and modulation of a 2DEG at the BFO/STO interface.

UV light induces oxygen vacancies in the STO, forming a quantum well that traps electrons to create the 2DEG. The polarization of the BFO layer, enhanced by UV illumination, further deepens this quantum well, increasing the carrier density and conductivity. Applying an external electric field can modulate these effects, allowing for control over the 2DEG properties, which is crucial for potential optoelectronic applications (Laohana et al., 2022).

2.3.2 Effects of oxygen vacancy

Oxygen vacancies are the most common defect in certain metal oxides and play a crucial role in electrical conductivity (Tanaka et al., 2002). In metal oxides, light exposure can create oxygen vacancy states between the valence and conduction bands. Research by Suwanwong et al. showed that 2DEG states form on the UV-irradiated surface of single crystal STO (100). UV light causes oxygen vacancies in STO, changing its resistance (Suwanwong et al., 2015). These 2DEG states contribute significantly to surface conductivity. To measure resistivity, a setup with gold electrodes in an interdigitated pattern was used, as shown in Figure 2.14(a). Before UV exposure, the resistance of the STO sample at 2×10^{-8} mbar was around 4 GΩ. Under UV light, the creation of 2DEG reduced the resistance to below 10 MΩ. When the UV light was turned off, the resistance gradually returned to its initial state, although more slowly, due to the persistent 2DEG. This behavior over time is similar to the ARPES data shown in Figure 2.11. Additionally, Jaiban et al. conducted a measurement of conductance on STO under UV light with a wavelength of 405 nm. The light was applied between two gold electrodes that were positioned 2 mm apart, as shown in Figure 2.14(b).

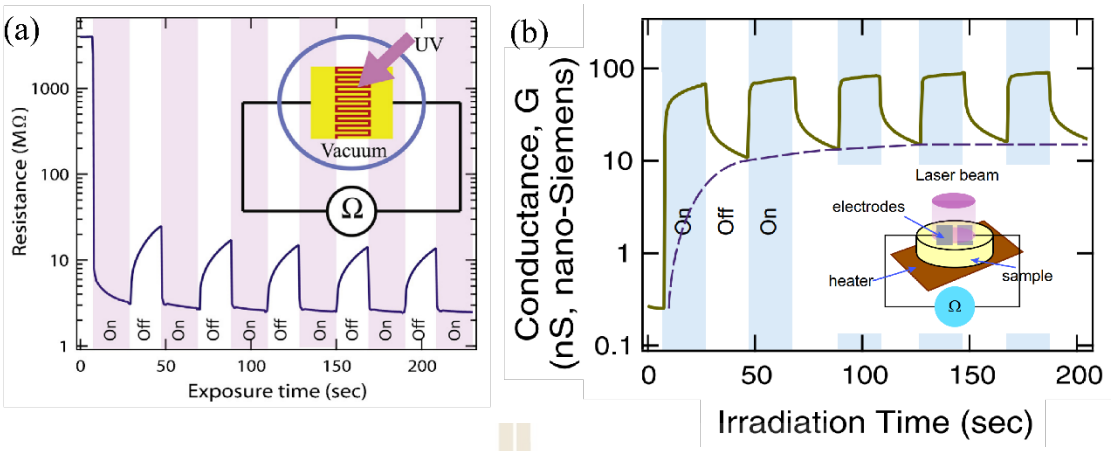

Figure 2.14 The resistance of the STO surface was measured during the on-off UV irradiation. The measurement setup diagram is shown in the inset figure. Study by (a) Suwanwong et al. (Suwanwong et al., 2015) and (b) Jaiban et al. (Jaiban et al., 2020), provide the details of these measurements and setups, respectively.

The conductance in the off state, influenced by the slow changing 2DEG, increased with longer exposure times, matching the increase in surface carrier densities seen in ARPES data (Jaiban et al., 2020). These findings highlight the significant impact of 2DEG on resistance and conductance changes. In 2024, Siwat Polin conducted a study to examine the magneto-optical Kerr effect (MOKE) in monodomain BFO thin films. The research focused on the impact of applied electric fields and light irradiation. The results show that the Kerr rotation of BFO changes under these conditions, indicating the ability to control the Kerr rotation using both electric fields and light irradiation.

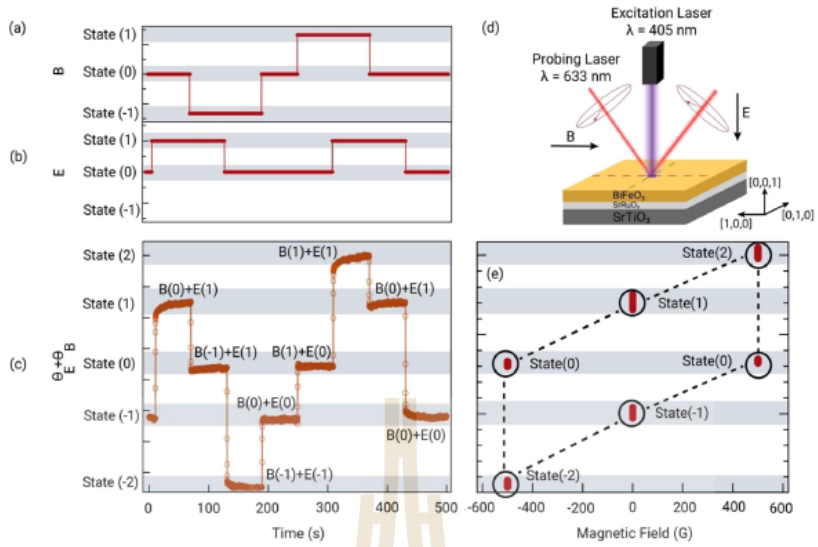

Figure 2.15 Coupling Mechanism between magnetic field and electric field or UV light via Kerr angle measurements in BFO films. (a) an applied magnetic field in units of Gauss and (b) an electric field or UV-light irradiation in units of W/m^2. (c) Changes in the Kerr angle ($\theta_B + \theta_E$) obtained from the applied magnetic field and electric field or UV-light irradiation. (d) A schematic illustrating the interaction between the magnetic field and the electric field or UV light through the Kerr-rotation measurement of the BFO film. (e) Changes in the states of BFO when an electric field, UV light, and a magnetic field are added or removed, measured in units of the Kerr angle. (Polin et al., 2024).

The Kerr angle in BFO thin films is influenced by the creation of oxygen vacancies, which enhance electrical polarization and modify magnetic properties. UV irradiation generates these vacancies, leading to a photo-voltage effect that increases polarization. This increased polarization interacts with the magnetic field, changing the Kerr angle. Figure 2.15 highlights the potential for using BFO in multifunctional devices that leverage the coupling between electric, magnetic, and optical properties (Polin et al., 2024).

CHAPTER III
RESERCH METHODOLOGY

This chapter covers preparation of the sample ranging from the preparation of the substrate, thin film deposition and nanopatterning to basic characterization. Both nano-grid patterned by FIB and gold nanohole array patterned by EBL are well defined. Additionally, the principal information and procedures from each experimental technique are described.

3.1 Substrate preparation

3.1.1 Substrate Cleaning

In this work, Nb-$SrTiO_3$ (NSTO) substrates (10 x 10 x 1.0 mm^3, [010],[001] orientation, one side polished from Crystal Base Co., Ltd) and Fluorine-doped Tin Oxide glass (FTO) were used. The NSTO and FTO were cut into sizes of 5.5 x 1.0 mm^2 and 10 x 10 x 2.2 mm^3, respectively. The cleaning process involved 4 steps. First, the substrates were cleaned with acetone to remove organic impurities. Then, they were rinsed with isopropanol (IPA) to get rid of any acetone residue, preventing streaks. After that, a rinse with DI water was performed. For each step, ultrasonic cleaning was applied to the NSTO and FTO for 15 minutes. After cleaning, the substrates were thoroughly dried. Nitrogen gas was used for drying. Water molecules, usually present due to cleaning process and air humidity, were removed by heating at 120°C for 1 hour. Finally, oxygen plasma cleaning (electronic diener plasma-surface technology) was used to clean the surfaces for removing organic and carbon contaminants, using 300 watts for 30 minutes at a pressure of 0.8 mbar.

3.2 Thin film deposition and nanoscale patterning

3.2.1 $BiFeO_3$ thin film deposition

The BFO films (a two-inch-diameter BFO target from Kurt J. Lesker Company, USA) were deposited on an NSTO substrate and FTO glass, each with a thickness of about 100 nm, using RF magnetron sputtering. Argon and oxygen gases flowed during the entire deposition process at a ratio of 4:1. The deposition was carried out under base and operated pressures of 3.6 and 6.0 mTorr, respectively. The RF power was set at 100 watts. The BFO film deposition began after 5 minutes of pre-sputtering, and the entire coating process was completed in 3 minutes without heating the substrate. Thermal annealing was performed in an air environment at a temperature of 600°C. The muffle furnace's heating rate was 5°C per minute. Once the temperature of each sample reached the target temperature, it was maintained for 30 minutes, and then the samples were allowed to cool down naturally at a rate of 5°C per minute to room temperature.

3.2.2 Nanoscale patterning of Metal oxide thin film.

3.2.2.1 Nano-grid pattern BFO/NSTO with Focus Ion Beam (FIB)

FIB technology is a key tool in nanotechnology for machining materials with high precision at the nanoscale (Orloff et al., 2003). FIB is mainly used for imaging, milling, deposition, and creating patterns on a very small scale (Yao, 2007). This technology enables the creation of tiny features, making it vital in fields like materials science, semiconductor research, and nanofabrication (Giannuzzi et al., 2005). FIB can produce nano-patterns as small as 5-10 nanometers, providing the precision and control needed for making advanced nanoscale devices and structures (Yao, 2012). The principle of FIB involves the use of a focused beam of ions, typically gallium ions, to interact with the surface of a sample (Orloff et al., 2003). The ions are accelerated and focused into a narrow beam, which can be directed with high precision onto the sample's surface. The interaction between the ions and the sample material results in the sputtering of atoms from the surface, allowing for the removal or deposition of

material with nanometer accuracy (Yao, 2007). This process can be controlled to create intricate patterns, such as grid patterns, by scanning the ion beam across the sample according to a predefined design (Giannuzzi et al., 2005).

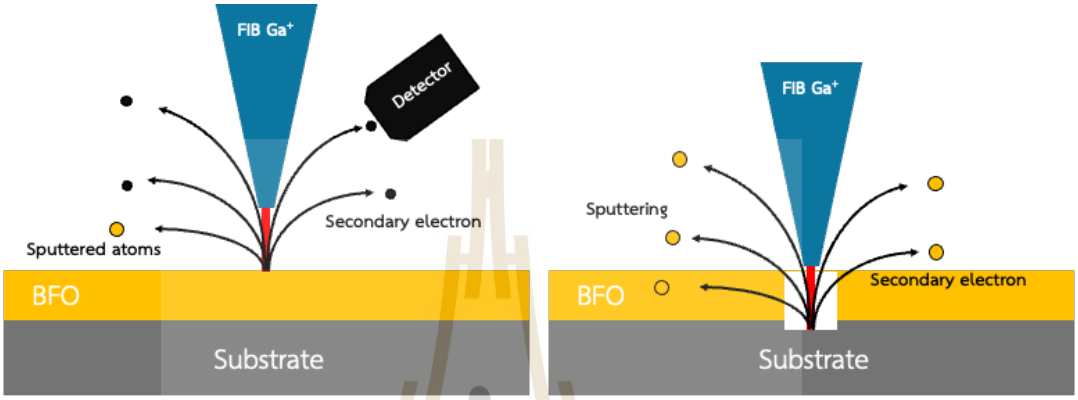

Figure 3.1 Diagram illustrating the principle of FIB operation.

In this study, FIB was chosen for creating grid patterns ranging from 200 to 2000 nm because of its accuracy and flexibility (Yao, 2012). Our system has both electron and ion beams, allowing real-time monitoring of the etching process. The acceleration voltage was set at 30 kV, and the ion current was 200 pA (matching a 30 nm spot size), based on the grid size. The ion beam was angled at 90° to the etched surface. After the FIB process, the sample was annealed again under the same conditions as the initial annealing. This step was to remove Gallium ions and restore the crystallinity of the structures (Orloff et al., 2003).

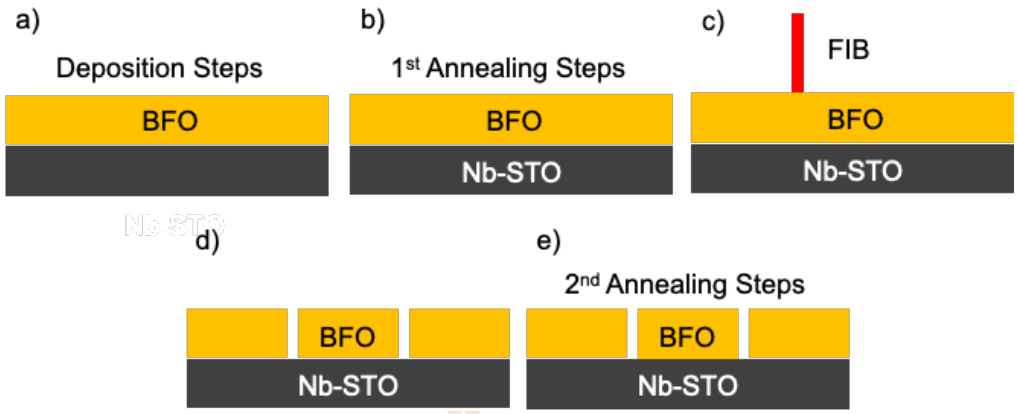

Figure 3.2 Schematic of the BFO film on NSTO fabrication procedure. (a) Deposition BFO thin film by RF-sputtering, (b) The Annealing with temperature at 600 °C, (c) the process of patterning, d) structures are acquired (e) Thermal treatments are designed to restore the crystalline nature of the structures and Gallium ion removal.

3.2.2.2 Au-Nanohole Array/BFO/FTO by Electron beam lithography (EBL)

EBL is a widely used technique in nanotechnology for creating very small patterns on a substrate. It is a key method in the fabrication of nanoscale devices due to its high precision and flexibility (Chen et al., 1993). EBL is commonly used in research and industry for producing intricate structures that are essential in various fields, including semiconductor manufacturing, materials science, and nanoelectronics (Rai-Choudhury, 1997). The principle of EBL involves using a focused beam of electrons to draw patterns on an electron-sensitive film called resist, which is coated on the substrate (Tseng, 2005). The electron beam changes the chemical structure of the resist in the exposed areas. This alteration makes the exposed areas either more or less soluble in a developer solution, depending on whether a positive or negative resist is used. This selective solubility allows for the precise creation of patterns at the nanoscale (Chen et al., 1993).

In this work, the process of creating nanostructures using EBL can be broken down into several steps. The first step is to apply a thin, even layer of electron beam resist onto the substrate using a spin coater. The negative electron beam resist (AR-N 7520 new e-beam resists). The spin coat condition is 4000 rpm for 45 seconds. This step ensures a uniform and thin layer of resist across the substrate. Soft bake on hotplate at 85℃ for 1 minute. Next, the sample is placed in an EBL system where a focused electron beam is used to write the desired pattern onto the resist. The e-beam changes the solubility of the resist layer in the exposed areas, defining the pattern. After exposure, post-bake at 85 ℃ for 1 minute on the hotplate. After exposure and post-bake, the sample is immersed in a developer solution. This step removes the resist in the unexposed area out, revealing the pattern (Chen et al., 1993). A thin layer of Chromium and gold are deposited over the entire substrate using methods like electron beam evaporation with the thickness 20 and 150 nm, respectively. This layer forms the needed structure. Then, the sample undergoes a lift-off process where the resist, along with the material deposited on top of it, is removed. This leaves behind the material only in the patterned areas. Finally, the sample is annealed at a specific temperature at 120℃ for 1 hour to improve the adhesion and quality of the deposited material, ensuring the stability and functionality of the nanostructures.

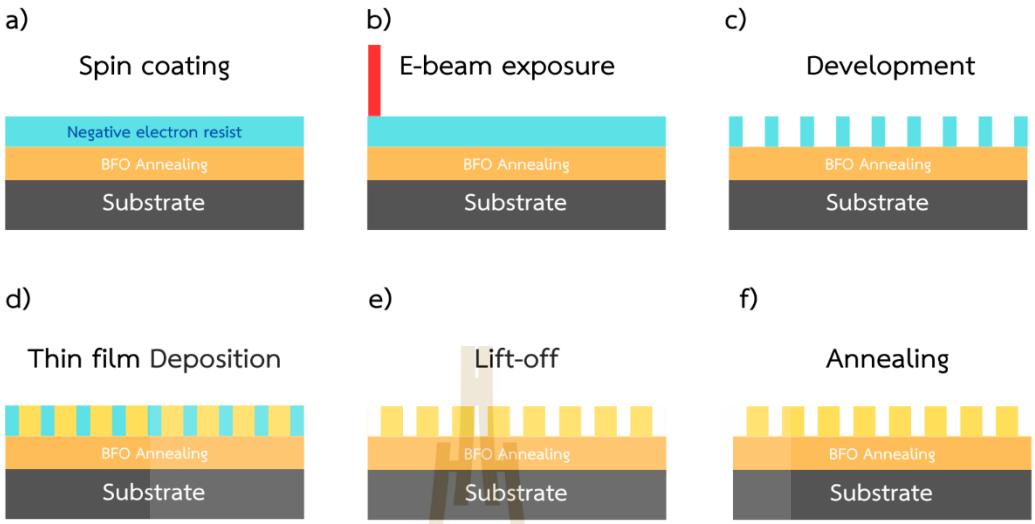

Figure 3.3 The process for direct writing using EBL: (a) The electron beam resist is applied to the surface of the substrate using spin coating. (b) A pattern is designed and then exposed onto the resist layer using an electron beam. (c) The sample undergoes a development process where the resist layer in the unexposed areas is removed, leaving behind the desired nanostructure pattern on the sample. (d) A thin layer of gold is deposited onto the patterned resist layer by electron beam evaporation. (e) The resist, along with the unwanted gold, is lifted off from the sample, revealing the gold pattern on the sample. (f) The sample is annealed at 120°C for 1 hour. This step helps to improve the crystallinity and adhesion of the gold layer to the substrate.

3.3 Basic characterization

3.3.1 X-ray diffraction (XRD)

XRD is a technique that is used to analyze the structure and composition of materials. Many researchers in materials science, chemistry, geology, and biology use it (Cullity et al., 2001). XRD works by shining X-rays onto a crystal sample. The X-rays are made in an X-ray tube, where a heated metal filament makes electrons. These electrons are shot at a target, making the target give off X-rays (Klug

et al., 1974). When the X-rays hit the sample, they bounce off in different directions depending on the crystal's atomic arrangement. We can look at this pattern to understand the crystal structure (Pecharsky et al., 2003).

The angle at which the X-rays bounce is important. We can use it to find the space between atomic planes. We do this using Bragg's law as shown in Figure 3.4 and equation (3.1):

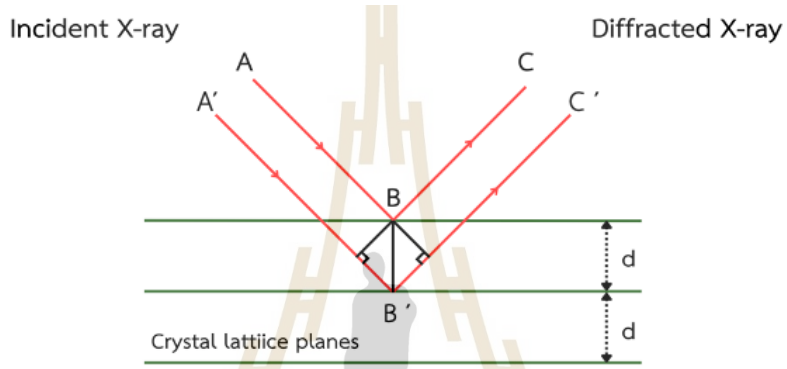

Figure 3.4 The illustration presents principal of X-ray diffraction.

$$\sin\theta = \frac{n\lambda}{2d} \tag{3.1}$$

where λ is the wavelength, θ is the angle of diffraction, and d is the distance between atomic planes.

The result of an XRD measurement is a graph of signal intensity against angles of diffraction, known as two theta positions. These positions show specific spacings between crystals or atoms in the sample (Cullity et al., 2001). By converting the diffraction peaks to d-spacings, we can identify minerals, as each mineral has unique d-spacings. This is usually done by comparing the d-spacings with standard patterns (Klug et al., 1974). XRD provides a lot of information. It tells us about chemical composition, crystal structure, crystal orientation, crystallite size, lattice strain, preferred orientation, and layer thickness. For larger crystals, XRD can find the atomic structure. For small crystals, XRD can determine the sample's composition, crystallinity,

and phase purity (Pecharsky et al., 2003). In this study, XRD was used to find out the crystal structure of different samples. These samples were: NSTO substrate, BFO on NSTO, BFO on NSTO and then annealed, FTO glass, BFO on FTO glass, BFO on FTO glass and then annealed. The XRD results were shown as intensity against a 2θ range from 20° to 80°.

3.3.2 Scanning electron microscope (SEM)

SEM is a method that helps us look closely at the surface of materials at the micro and nano scale. It is used in many research fields like materials science, chemistry, geology, and biology (Burany, 2003; Egerton, 2005). The basic idea of SEM is to use a strong beam of high-energy electrons that hit the atoms in the sample. As these electrons move across the sample's surface, they scatter. The slower secondary electrons are collected by a detector and used to create a magnified image of the sample. This gives a detailed view of the sample's surface (Reimer, 1998; Williams et al., 2013). In our research, SEM is used to compare the surface of different samples. Here are some general observations we might make as demonstrated in Table 3.1.

Table 3.1 Sample's condition list for SEM measurement.

Name	Substrate	Deposited Thin Film	Annealing process (°C)
NSTO substrate	NSTO	-	-
BFO on NSTO	NSTO	BFO	-
BFO on NSTO annealed	NSTO	BFO	600
FTO glass	FTO	-	-
BFO on FTO	FTO	BFO	-
BFO on FTO annealed	FTO	BFO	600

3.3.3 Optical profilometer

The optical profilometer is an important tool in surface metrology. It uses light to measure a surface's topography without touching it (De Groot, 2015). The optical profilometer works based on light interference. Light from a source is split into two paths by a beam splitter. One path goes to the test surface, and the other goes to a reference mirror. The reflections from these surfaces are combined and sent to a digital camera. When the path lengths are within a few light wavelengths, interference patterns form. These patterns show details about the sample surface's shape. The data from the profilometer gives detailed information about the surface's topography. This includes surface roughness, flatness, warpage, and step-height (Thomas, 1999). The data can also be used for advanced measurements of critical dimensions. The information from the profilometer helps us understand the sample surface's geometric features, such as height differences, slopes, curvature, and irregularities.

In this research, an optical profilometer was used to measure the thickness of thin films after coating and the electron beam resist during nanoscale sample preparation (Bhushan, 2010). The profilometer's non-contact, high-resolution measurements are important for controlling film and resist thickness, which affects their properties and the success of electron-beam lithography. Therefore, the optical profilometer is essential for both the coating process and nanoscale sample preparation.

3.3.4 Energy-Dispersive X-ray Spectroscopy (EDS)

EDS is a method used to find the chemical composition of a material. Each element has a unique atomic structure, which creates distinct peaks in its emission spectrum (Burany, 2003). The process starts when a beam of X-rays hits the sample. This beam can knock an electron out of one of the inner shells of an atom, creating a vacancy. An electron from an outer shell then fills this vacancy, and the energy difference is released as an X-ray (Egerton, 2005). The emitted X-rays have energy that is characteristic of the element they came from. These X-rays are detected,

and their energy is measured, allowing us to identify and measure the elements in the sample (Reimer, 1998). The main parts of an EDS system include the excitation source (either an electron or X-ray beam), the X-ray detector, the pulse processor, and the analyzer. The type of excitation source depends on the application: electron beam excitation can be found in electron microscopes, including scanning electron microscopes (SEM) and scanning transmission electron microscopes (STEM) (Williams et al., 2013). EDS is a non-destructive technique, making it valuable in many research fields. It is often used with SEM to give detailed information about the elemental composition of materials (Fultz et al., 2008). In our thesis, we used EDS to find the elements and their percentages composition in the thin film sample.

3.3.5 Piezoresponse Force Microscopy (PFM)

PFM is a specialized scanning probe microscopy technique used to study the piezoelectric properties of materials at the nanoscale. It is especially useful for examining ferroelectric domains and their dynamics, which are important in materials science, electronics, and nanotechnology (Kalinin et al., 2006). PFM works by applying an AC voltage to a conductive tip that is in contact with the sample's surface. This voltage causes the material to deform due to its piezoelectric properties. The deformation is detected by the AFM cantilever, which is used to map the piezoelectric properties of the sample (Alexe et al., 2004). PFM relies on the inverse piezoelectric effect, where an applied electric field causes a mechanical strain in the material. The amplitude measures the magnitude of the sample's deformation in response to the applied voltage, indicating the strength of the piezoelectric response (Gruverman et al., 2006). The phase measures the phase difference between the applied AC voltage and the resulting mechanical response, providing information on the orientation of ferroelectric domains (Neumayer et al., 2020). Additionally, the topography maps the surface topography of the sample simultaneously with the PFM measurements using the AFM. We can use the simultaneously obtained topographical data to correlate surface features with piezoelectric properties, helping to understand how structural characteristics influence piezoelectric behavior (Kalinin et al., 2006).

3.3.5.1 Sample configurations for PFM measurement

Proper sample preparation is crucial for obtaining reliable and accurate PFM measurements. This section outlines the steps taken to prepare BFO thin films on a NSTO substrate and FTO glass for PFM analysis.

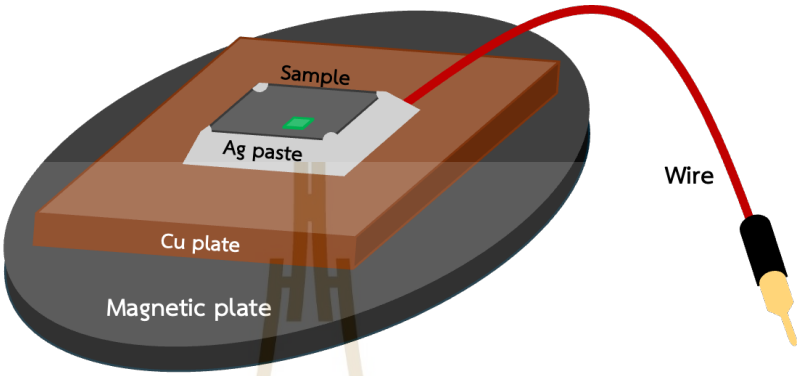

Figure 3.5 The sample preparation for PFM measurement.

Firstly, the sample was cleaned to remove any surface contaminants. This can be done using solvents such as acetone and isopropyl alcohol (IPA) rinsing the sample sequentially in acetone and IPA. Then, it was dried using nitrogen gas flow. Secondly, mounting the sample to secure the sample on a copper plate using conductive adhesive. This step ensures that the sample is firmly attached and has a good electrical connection with the copper plate. To ensure good electrical contact, a small region of the sample is painted with silver paste. Applying the silver paste to a corner of the sample will act as an electrode to facilitate the application of an electric field during PFM measurements. Then, the electrical wires were attached to copper plate to establish an electrical connection to the external voltage source during PFM measurements. Also, another wire should be connected to the silver-painted conner to complete the electrical circuit. Lastly, samples need to be held on the magnet plated for connecting with the PFM sample state. The complete look of the sample which is ready for PFM measurement is illustrated in Figure 3.5.

3.3.5.2 PFM amplitude and phase measurement

In this study, Piezoresponse Force Microscopy (PFM) was employed to investigate the ferroelectric properties of BFO thin films deposited on a NSTO substrate and FTO glass. PFM is a powerful technique for characterizing ferroelectric property on a nanoscale level, offering insights into domain structures and their dynamics. Using PFM, we measured both the phase and amplitude responses of the BFO thin films. The conductive AFM tip (Multi75E-G from budgetsensors) was used to apply an AC voltage (17 kHz, 2.5 Vpp) to the sample surface, inducing a piezoelectric response. The AFM cantilever detected the resulting deformation, allowing us to map the phase and amplitude across the sample. The phase response provided information on the orientation and polarity of the ferroelectric domains.

Figure 3.6 The phase image shows different polarization direction when voltage is applied to the sample surface.

By analyzing the phase data, we were able to identify regions with different domain orientations. The amplitude response indicated the magnitude of the piezoelectric effect, reflecting the strength and uniformity of the ferroelectric properties across the sample (Gruverman et al., 2006). To further investigate the ferroelectric behavior, a DC voltage was applied to the surface of the BFO/NSTO and BFO/FTO sample. This application allowed us to study the switching behavior of the ferroelectric domains. By applying a series of positive and negative voltages, we induced domain switching and observed the changes in both phase and amplitude responses. This experiment was crucial for understanding the stability and reliability of the ferroelectric properties under an applied electric field.

3.3.5.3 PFM amplitude and phase measurement under UV

In this study, we utilized a modified PFM setup to measure the piezoelectric properties of the sample under UV irradiation. The setup is based on the standard PFM configuration with an additional blue laser to illuminate the sample during measurements. The blue laser with a wavelength of 405 nanometers was used and the beam spot was focused on the area being scanned by the AFM tip. The intensity of the blue laser was set at 4.5 volts. PFM measurements were conducted with and without UV irradiation which can be compared later to ensure the effect of UV irradiation.

3.3.5.4 PFM hysteresis measurement

PFM hysteresis loop measurements are essential for investigating the ferroelectric properties of materials, especially their polarization switching behavior.

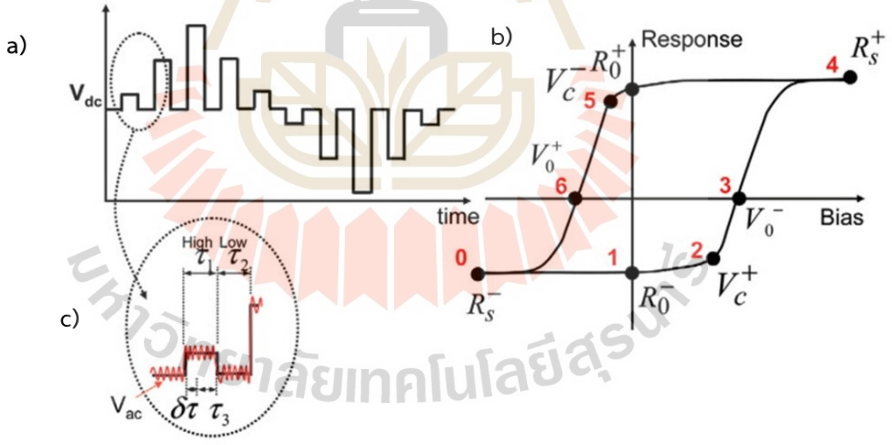

Figure 3.7 The switching spectroscopy PFM: (a) DC triangle waveform, (b) local hysteresis loop result, and (c) the zoomed-in view of triangle waveform (Kalinin et al., 2008).

The hysteresis loop provides valuable information about the material's coercive field, remanent polarization, and domain dynamics (Kalinin et al., 2008). The experimental setup is also based on conventional PFM with external data

acquisition (DAQ) and waveform generator to operate switching spectroscopy PFM as shown in Figure 3.7.

For the measurement procedure, the PFM system was used to map the position of the area of interest on the sample. This ensures precise targeting of the region where the hysteresis loop will be measured. The DC triangular waveform from the waveform generator was set with the maximum of +10V and minimum of -10V, then it applied to the AFM tip. The AC reference signal of 17 kHz frequency with 2.5 V peak-to-peak (V_{pp}) was applied to the sample. The combined external voltage bias is illustrated in Figure 3.7(a) and Figure 3.7(c). The amplitude and phase of the piezoresponse were detected by the system and passed through a lock-in amplifier. Then, external DAQ was used to record the amplitude, phase, and applied voltage signals. To clearly demonstrate the data, only the average of signals on the DC off-field region were selected. Amplitude and applied voltage plot show the amplitude of the piezoelectric response as a function of the applied DC voltage, revealing the characteristic butterfly loop which indicates polarization switching. Phase and applied voltage plot show the phase response as a function of the applied DC voltage, forming a hysteresis loop that provides insights into the polarization direction and switching dynamics. In addition, with the result of amplitude and phase, the piezoresponse can be calculated by equation (3.2) (Neumayer et al., 2020).

$$PR = A\sin\emptyset \tag{3.2}$$

where (A) is the amplitude of the response and (ϕ) is the phase angle. This calculation is performed for each data point as a function of the applied voltage.

The calculated piezoresponse values were plotted against the applied voltage to generate the hysteresis loop as illustrated in Figure 3.5(b). From the hysteresis loops, ferroelectric properties such as coercive field, the voltage at which

polarization switching occurs, remanent polarization, the polarization after removing the applied field, and other domain switching behaviors were analyzed.

The PFM hysteresis loop measurement setup, enhanced with an external Data Acquisition (DAQ) system, allows for precise and detailed investigation of the ferroelectric properties of materials. By mapping the area of interest, applying controlled waveforms, and utilizing a lock-in amplifier in conjunction with a DAQ system, we can accurately measure and analyze the piezoresponse of the sample under varying applied voltages. This approach provides comprehensive insights into the material's polarization switching behavior and ferroelectric characteristics.

CHAPTER IV
RESULTS AND DISCUSSION

This chapter presents the results from two distinct samples: BFO on NSTO and a Gold Nanohole Array (AuNHA). The characteristics and properties of these materials were investigated using various techniques to examine the impact of nano-patterning. Additionally, the effect of UV irradiation on ferroelectricity is discussed.

4.1 Basic characterization

4.1.1 X-ray diffraction (XRD)

XRD was used to analyze the crystal structure of 7 different samples, including NSTO, FTO, BFO/NSTO, BFO/FTO both before and after annealing, and AuNHA sample. The main peaks of NSTO and FTO were visible in all samples. The unannealed BFO samples showed an amorphous phase with peaks at 2θ angles of 22.5° (100), 45.6° (200), and 71.4° (300). After annealing, the BFO films showed clear crystal formation at the same 2θ positions, with higher intensity and sharper peaks compared to the unannealed samples. This indicates that the BFO thin films formed crystalline structures on NSTO (100) single crystals and FTO substrates when processed by RF magnetron sputtering and heated at 600°C for 30 minutes. However, impurity phases from the NSTO and FTO substrates, caused by diffraction of Cu-Kβ radiation, were observed and marked with a "*" symbol.

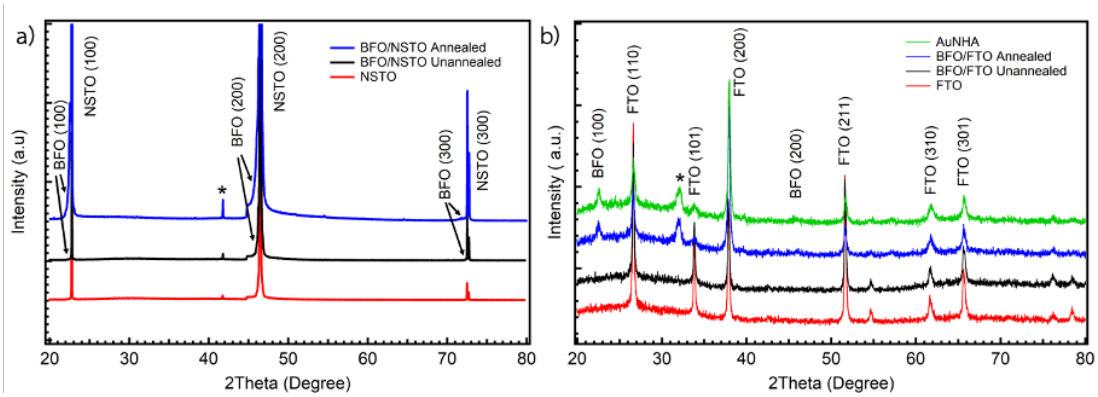

Figure 4.1 (a) shows the XRD patterns of NSTO, BFO/NSTO unannealed and annealed samples. (b) shows the XRD patterns of FTO, BFO/FTO unannealed and annealed samples, and AuNHA. The figure displays the (100), (200), and (300) diffraction peaks of BFO films on both substrates.

4.1.2 Scanning electron microscope (SEM)

SEM was used to observe the surface morphology of six sample conditions. The SEM high voltage was set at 20.0 kV for all images to ensure comparability. The images were taken with a magnification of 50 kx. For the NSTO substrate before adding any BFO, the surface appeared very smooth with no visible structures. This indicates that the NSTO was clean without crystal formations. Similarly, for the unannealed BFO/NSTO sample, the surface remained smooth, as illustrated in Figure 4.2(a) and Figure 4.2(b). This suggests that the BFO layer was thin and did not develop a crystalline structure. In contrast, the BFO/NSTO sample after annealing at 600°C for 30 minutes exhibited the crystallization on BFO thin film, suggesting that the heating process improves the formation of crystals as demonstrated in Figure 4.2(c).

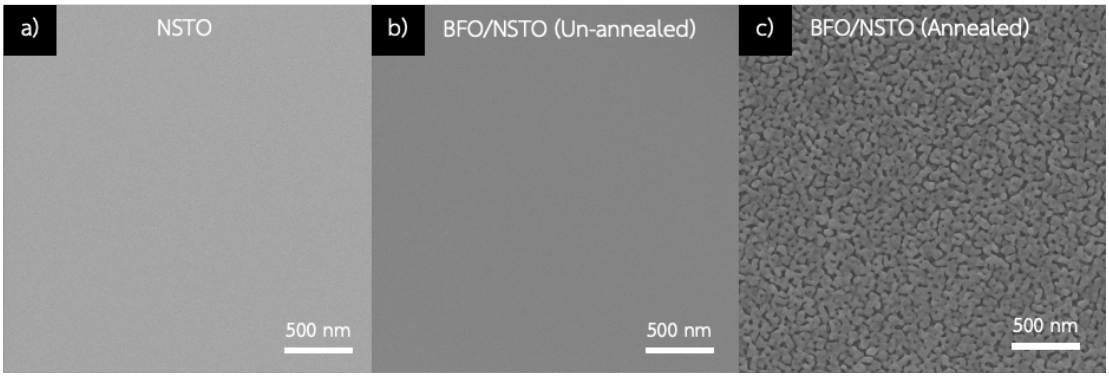

Figure 4.2 SEM images of (a) NSTO substrate, (b) BFO/NSTO sample in the RT condition with 3 minutes deposition time, (c) BFO/NSTO after annealing. The scale bar represents the length of 500 nanometers.

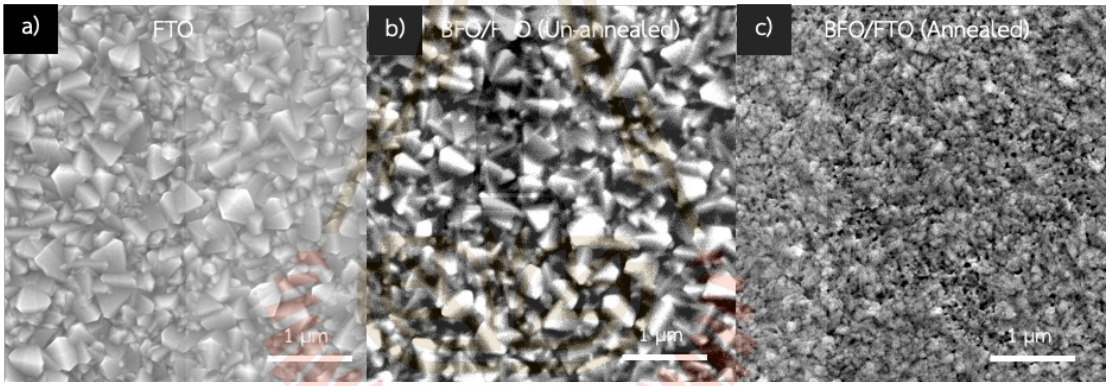

Figure 4.3 SEM images of (a) FTO substrate, (b) BFO/FTO sample in the RT condition at a deposition time of 3 minutes, (c) BFO/FTO after annealing. The scale bar represents the length of 1 micrometer.

For the FTO substrate samples, SEM images were taken at a magnification of 20 kx, and the high voltage was set to 10.0 kV. The surface morphology of the FTO substrate showed a grainy structure with well-defined grains (Figure 4.3(a)). This is typical for FTO glass, where the grains are relatively uniform in size and shape. The surface morphology of BFO deposited on FTO glass without annealing was more irregular and rougher compared to that of the FTO glass (Figure 4.3(b)). The grains appeared larger and less uniform, suggesting that the BFO layer was not well-

crystallized. In contrast, the surface morphology of BFO on FTO glass after annealing was smoother and more uniform compared to the unannealed sample. The grains were smaller and more evenly distributed, suggesting that the annealing process improved the crystallinity of the BFO layer (Figure 4.3(c)).

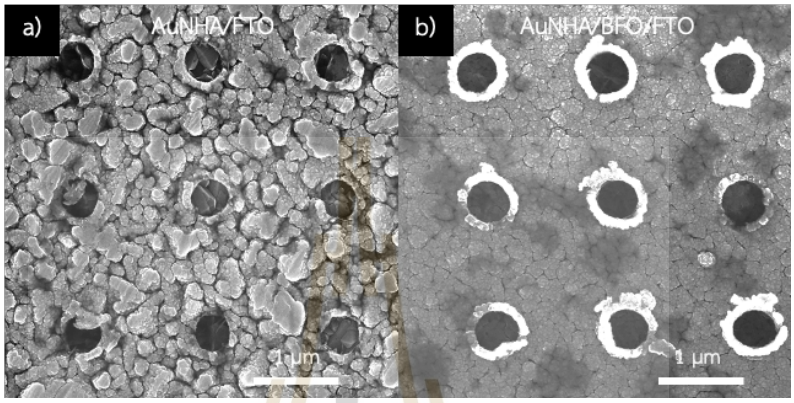

Figure 4.4 SEM images of AuNHA on (a) FTO substrate, (b) BFO/FTO sample in the RT condition at a deposition time of 3 minutes. The scale bar represents the length of 1 micrometer.

The surface morphology of AuNHA/FTO and AuNHA/BFO/FTO samples was observed using SEM images with a high voltage setting of 30.0 kV and a magnification of 30 kx. The nanoholes were arranged in a regular pattern, consistent in size and shape, indicating a precise and controlled fabrication process. The average size of the holes on FTO was 446 nm (Figure 4.4(a)). While the nanoholes of the AuNHA/BFO/FTO sample had an average hole size of 493 nm, as illustrated in Figure 4.4(b).

4.1.3 Field emission scanning electron microscope (FESEM)

After the sample preparation process, we used FIB to create grid patterns with size 200-2000 nm. For the PFM study, a dimension of 300x400 nm² was used because this size closely matches the AuNHA sample. The polarization on the surface is most clearly observed at this size. The acceleration voltage, ion current, and

depth were set at 30 kV, 200 pA, and 0.4 micrometers, respectively. The spot size of the probe was 30 nm. The ion beam was positioned at a 90 degrees angle to the surface being etched by rotating the sample stage by 54 degrees. FESEM was used to observe the surface morphology of the sample with SEM high voltage settings at 5.0 kV.

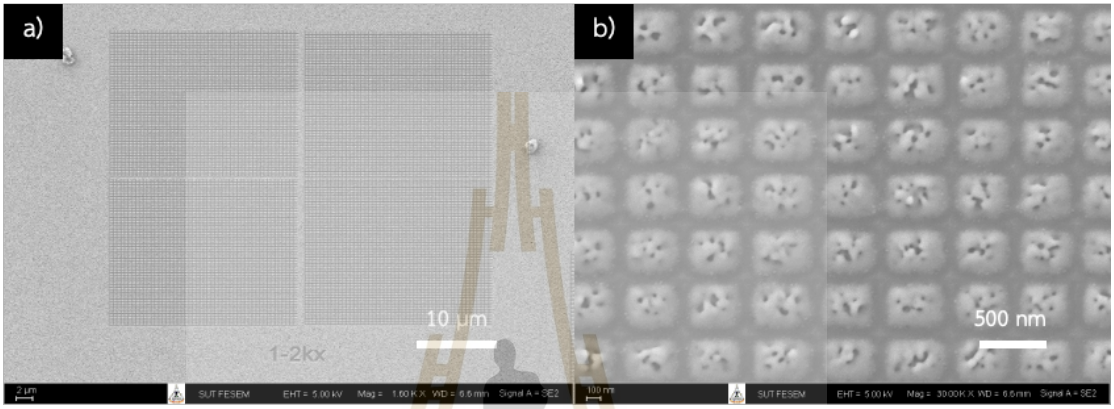

Figure 4.5 FESEM images after patterned nanostructures of unannealed BFO/NSTO. The magnified images of square-shaped nanostructures are shown at (a) 1.6 kx and (b) 30 kx. The patterning field size is 40 x 50 μm^2 and grids size is 300 x 400 nm^2. The scale bars represent 10 µm and 500 nm, respectively.

In figure 4.5(a), a nano grid pattern was created using FIB. The grid size is 300 x 400 nm^2, and the total patterned area is 40 x 50 μm^2. The grid was made with high precision and uniformity, demonstrating the capability of FIB to create small, accurate patterns. The overall area exhibits a well-ordered and consistent structure. A zoomed-in view of the same nano grid at a magnification of 30 kx as demonstrated in Figure 4.5(b). This close-up shows more details of the individual grid cells. Each cell appears uniform, although some imperfections are visible on the surface. These imperfections might be due to the deposition and annealing process. Despite these minor issues, the grid shows high precision and consistency, proving that FIB is effective for creating nanoscale patterns.

4.1.4 Energy dispersive X-ray spectroscope (EDS)

EDS was used to determine the weight and atomic percentages of elements in NSTO, BFO/NSTO, FTO, and BFO/FTO samples. The peaks in the graphs indicate the presence of elements in each sample. For the NSTO substrate, elements detected included Strontium (Sr), Titanium (Ti), Niobium (Nb), and Oxygen (O). Additionally, Bismuth (Bi) and Iron (Fe) were found in the BFO thin film on the NSTO substrate, both unannealed and annealed, with the weight and atomic percentages shown in Figures 4.6(a) to 4.6(c). For the FTO substrate, only Tin (Sn) and Oxygen (O) were found. Similar to the NSTO substrate, Bismuth and Iron were detected when the BFO layer was deposited on the FTO substrate, as illustrated in Figures 4.6(d) to 4.6(f). This confirms that the BFO layer was successfully deposited on both the NSTO and FTO substrates. Comparing the unannealed and annealed BFO/NSTO and BFO/FTO samples, there are slight differences in the weight and atomic percentages of the elements. The annealing process alters the material structure, affecting the distribution and percentage of elements.

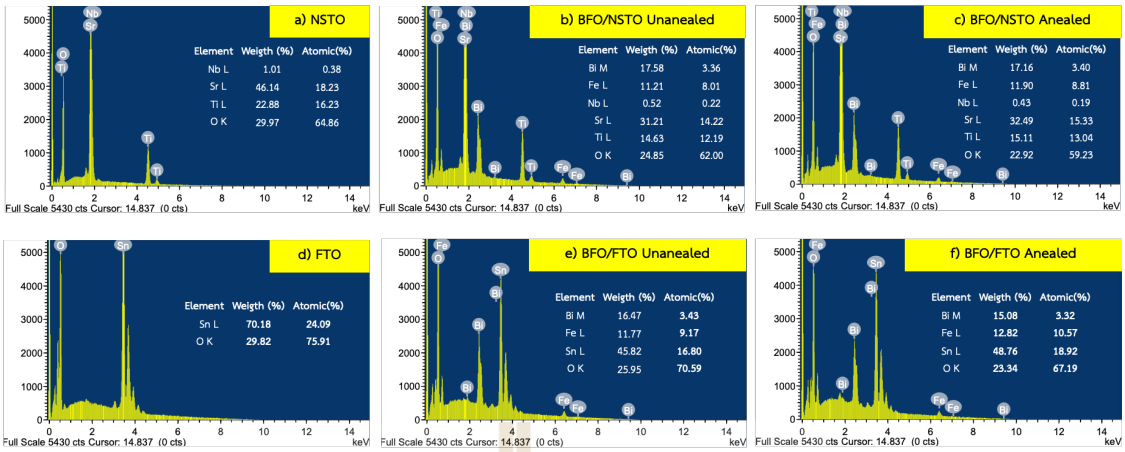

Figure 4.6 EDS elemental analysis of (a) NSTO substrate, (b) BFO/NSTO unannealed, (c) BFO/NSTO annealed, (d) FTO substrate, (e) BFO/FTO unannealed and, (f) BFO/FTO annealed.

4.2 Ferroelectric properties

To confirm the ferroelectric property, there are two effects that need to be checked. First, the domains should have different orientations of polarization. Second, there should be hysteretic switching between opposite domain states caused by electric fields. Hence, Piezo-respond Force Microscopy (PFM) was used in this experiment to study the ferroelectric properties of the BFO/NSTO and BFO/FTO samples and both un-patterned and patterned areas were studied. The tip applied voltage in the poling process was set to be +10V and -10V for all the PFM measurements. Additionally, we also studied the effect of UV irradiation on the ferroelectric properties.

4.2.1 Controlling the nano-scale ferroelectricity in unpatented area

To test the limitations of ferroelectricity control, we utilized PFM to create small-sized letters on a BFO/NSTO sample. In this experiment, we created the letters by applying a +10 V DC voltage over a 4 x 4 micrometer area and then applying -10 V to write the letters. After poling, the PFM amplitude and phase were investigated,

as shown in Figure 4.7. The PFM amplitude images show the letters "SUT" clearly visible, standing out from the background. The bright areas represent a strong response to the applied voltage, while the dark areas show a weaker response. The brightness ranges from 0 to 1.4 V, indicating the magnitude of polarization on the sample. The phase images display distinctly visible letters, representing changes in polarization direction, with phase values ranging from -80 to 80 degrees.

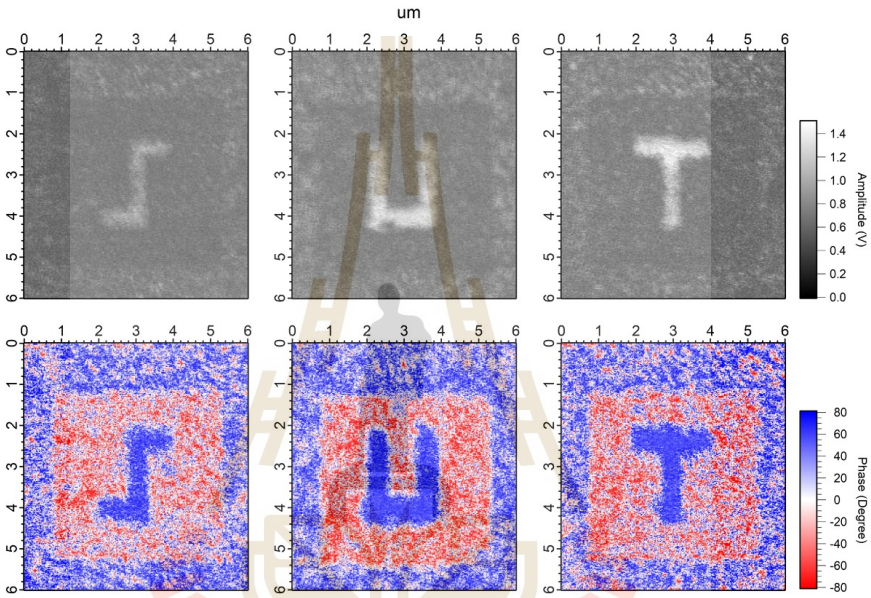

Figure 4.7 PFM images showing the nano-letter patterns on the BFO/NSTO annealed surface. The top row displays PFM amplitude images, and the bottom row shows PFM phase images. The letters S,U, and T were created by applying +10 V over a 4 x 4 micrometer area (red color) and then -10 V to form the letters, each approximately 500 nm wide (blue color). The scan size for each image is 6 micrometers.

From these experimental results, we conclude that we successfully used PFM to investigate these nano patterns and create tiny, polarized letters on the BFO/NSTO surface by applying different DC voltages. The letters are approximately 500 nm in size. The clear contrasts in the amplitude and phase images show that the electric fields effectively changed the local polarization states. The ability to create

and detect such small patterns can be useful for data storage and nano-electronic devices. It also aids in studying small-scale domain changes.

4.2.2 Effect of nanopatterning on ferroelectricity

For the un-patterned BFO/NSTO annealed sample, the hysteresis loop results and PFM images, including topography, amplitude, and phase, are shown in Figure 4.9. The topography image clearly shows the surface of the BFO film, identifying surface features of the sample (Figure 4.8(a)). The amplitude image distinctly shows different contrasts when an electric field is applied; higher amplitude indicates a stronger piezoelectric response. After poling, areas with different polarization states display varying amplitude levels, with magnitude ranging from 0 to 2.1 V (Figure 4.8(b)). The phase image effectively represents the direction of polarization. The contrast in phase helps identify areas with different polarization directions. After poling with +10V and -10V, distinct phase regions indicate domain switching (Figure 4.8(c)). The hysteresis loops for amplitude, phase, and piezo response over applied voltage are shown in Figures 4.8(d), 4.8(e), and 4.8(f), respectively. The amplitude loop shows the change in piezoelectric amplitude as the voltage is applied. The "butterfly" shape, typical of ferroelectric materials, demonstrates how the piezoelectric response changes with voltage, confirming the magnitude of polarization switching under an electric field. The phase loop shows the change in polarization direction as the voltage is applied. A typical ferroelectric phase hysteresis loop displays sharp phase changes, indicating the switch between polarization states. For the un-patterned area, the phase switched in the range from -80 to +80 degrees. The piezoresponse vs. applied voltage plot combines the amplitude and phase data to show the overall piezoelectric response of the sample. The results of this experiment reveal that BFO/NSTO annealed exhibits strong ferroelectric and piezoelectric properties in the un-patterned area, with clear domain switching and significant piezoelectric response under applied electric fields.

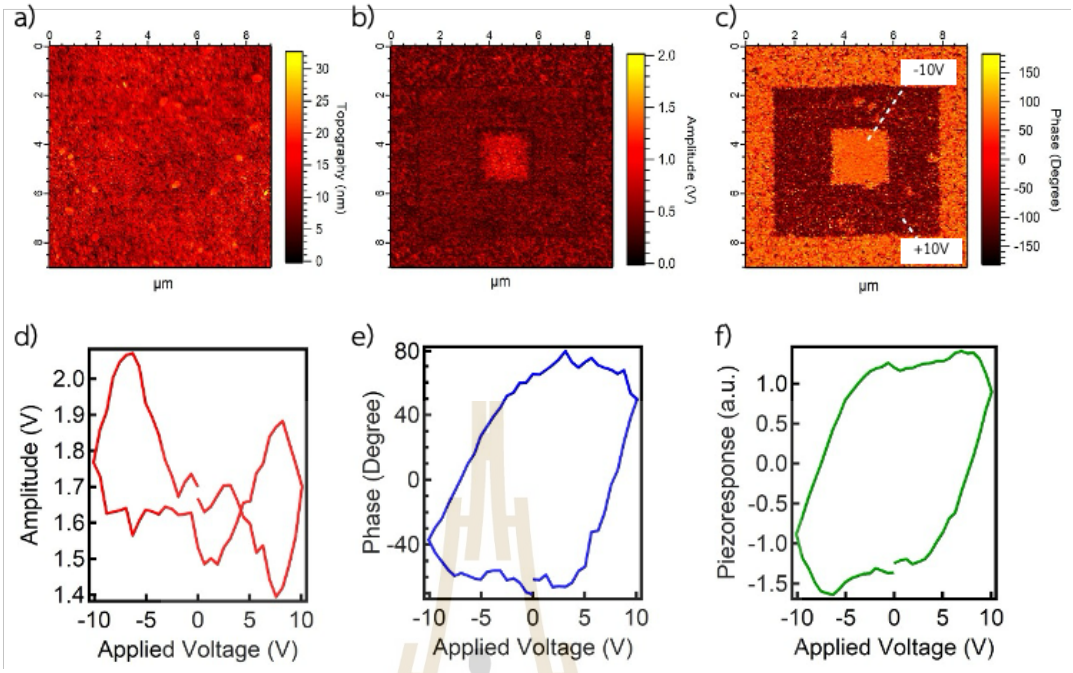

Figure 4.8 PFM Images for un-patterned area (a) the topography, (b) PFM amplitude, and (c) PFM phase images after poling with +10V and -10V DC voltages. The hysteresis loops of BFO/NSTO annealed in the un-patterned area (d) amplitude, (e) phase, and (f) piezoresponse as functions of applied voltage.

For the nano-scale grid patterned by FIB, Figure 4.9 presents the results of a PFM and hysteresis loop study on an BFO/NSTO annealed sample with a nano grid size of 400-500 nm. The topography image (Figure 4.10(a)) shows the surface features of the BFO film in a nano grid pattern, clearly indicating a well-defined structure created by the FIB technique. The grid features are approximately 300x400 nm^2 in size, with a height of around 80-100 nm. The amplitude image (Figure 4.9(b)) did not reveal clear contrast after poling, with the polarization magnitude measurable only in the range of 0-1.2 V. However, the phase image (Figure 4.9(c)), after applying +10V and -10V, displayed distinct phase regions, indicating successful domain switching within the grid pattern. The contrast in these phase regions confirms the presence of polarization domains. The hysteresis results, shown in Figures 4.9(d) to 4.9(f), confirm the ferroelectric properties of the nano grid pattern through the characteristic butterfly

shape in the amplitude and phase switching. The phase hysteresis loop shows a switch between positive and negative at around 60 degrees, which is less than the un-patterned area. Additionally, the clockwise rotation of this phase result compared to the unpatterned area indicates the involvement of an electrostatic field. The piezoresponse plot with the applied electric field further indicates ferroelectric properties in the nano grid pattern.

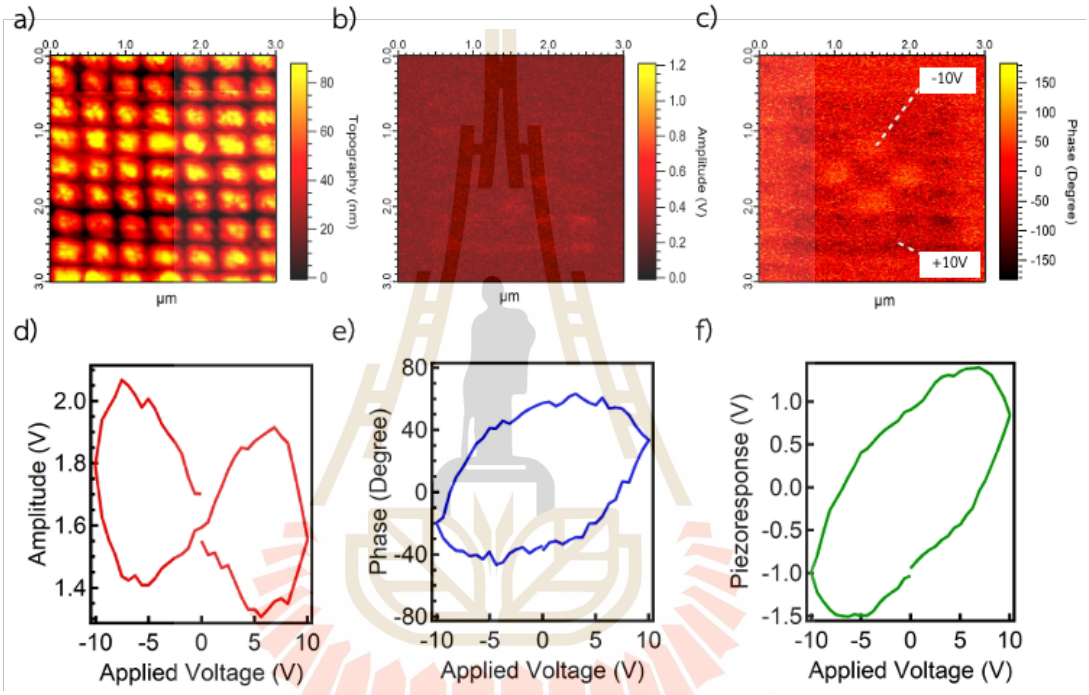

Figure 4.9 PFM and hysteresis loops of nano-grid BFO/NSTO. The top row displays (a) topography, (b) PFM amplitude, and (c) phase images after poling with +10V and -10V DC voltages on a grid. The hysteresis loops for (d) amplitude, (e) phase, and (f) piezoresponse over applied voltage.

For BFO/FTO annealed sample, topography Image (Figure 4.10(a)) reveals the surface features of AuNHA on BFO/FTO. The nanohole pattern is clearly visible, indicating successful fabrication of the nano-array with the average hole size of 493 nm. The amplitude (Figure 4.10(b)) and phase image (Figure 4.10(c)) represent the piezoelectric response of the sample only around the hole region. The contrast of

amplitude and the phase switching are not clear, suggesting low piezoelectric response across the nanohole array region. The PR curve combines amplitude and phase data to present the overall piezoelectric response of the sample. The piezoelectric responses of the material show smaller than 2 previous samples, demonstrating non-effective polarization switching within the nanohole array as illustrated in Figure 4.10 (e-f).

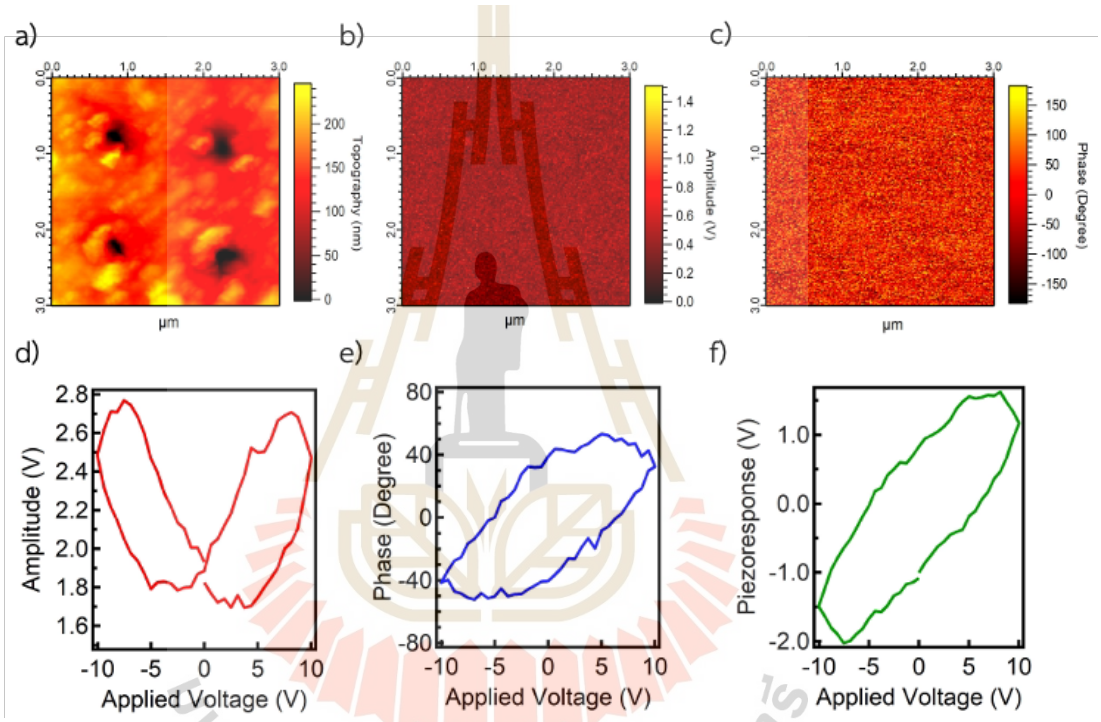

Figure 4.10 PFM and hysteresis loop AuNHA/BFO/FTO (hole size 493 nm). The top row displays (a) topography, (b) amplitude, and (c) phase images, revealing the surface features and polarization states after poling with +10V and -10V DC voltages. The hysteresis loops for (d) amplitude, (e) phase, and (f) piezoresponse vs. applied voltage.

Table 4.1 Ferroelectric coefficient.

Sample	Maximum Amplitude	Remnant Polarization (P_r)	Coercive Field (E_c)
Unpatterned Area	2.07 V	±1.2 V	±8.2 V
FIB Patterned Area	2.07 V	±0.9 V	±6.9 V
Nanohole Array Patterned Area	2.77 V	±0.83 V	± 6.3 V

The piezoelectric response and domain switching were observed in both the nanohole array and the FIB-patterned area. However, the unpatterned area exhibited a higher overall piezoresponse. From the piezoresponse hysteresis loops plot, we determined the remnant polarization and coercive field for these three areas, as shown in Table 4.1. The unpatterned area had larger piezoresponse values, but the patterned areas (both FIB and nanohole array) exhibited more consistent switching behavior.

4.2.3 Effect of UV irradiation on ferroelectricity

For this section, we will investigate the ferroelectric properties of an annealed BFO film on an NSTO substrate by measuring the PFM amplitude under three different UV irradiation states: state1 (No UV), state 2 (Under UV), and state 3 (After UV). Additionally, there are also three distinct areas (A1, A2 and A3) which extend it into nine conditions: ($A_{1,1}$) to ($A_{3,3}$) as illustrated in Table 4.2. The poling process was set to applied voltage -10 V and +10V into the sample. The average amplitude (mean) and standard deviation (SD) for each area were calculated and plotted against the UV states. All the results were shown in Figure 4.11 and Figure 4.12.

Table 4.2 UV irradiation conditions for -10V applied voltage.

State/Area	A1	A2	A3
1	Poling before UV ($A_{1,1}$)	-	-
2	Amplitude decay ($A_{1,2}$)	Poling with UV ($A_{2,2}$)	-
3	Amplitude decay ($A_{1,3}$)	Amplitude decay ($A_{2,3}$)	Poling after UV ($A_{3,3}$)

There are two sets of experiments: one with an applied voltage of -10V and the other with +10V. Firstly, the results in area A1 showed a significant drop in amplitude from 2.3V to 0.43V between conditions ($A_{1,1}$) and ($A_{1,2}$), indicating that UV exposure reduces the ferroelectric response. The amplitude then remains unchanged from condition ($A_{1,2}$) to ($A_{1,3}$). Notably, the amplitude of 0.63V in the ($A_{2,2}$) state suggests that the poling process under UV irradiation ($A_{2,2}$) is less effective compared to the poling without UV in the (A1,1) and ($A_{3,3}$) states. The amplitude slightly decreases from the ($A_{2,2}$) state to the ($A_{2,3}$) state, suggesting normal decay over time. Interestingly, the poling process after UV irradiation results in an amplitude increase similar to the ($A_{1,1}$) state, although the magnitude is slightly lower. This indicates that the ferroelectric properties do not fully recover to the initial state after UV exposure.

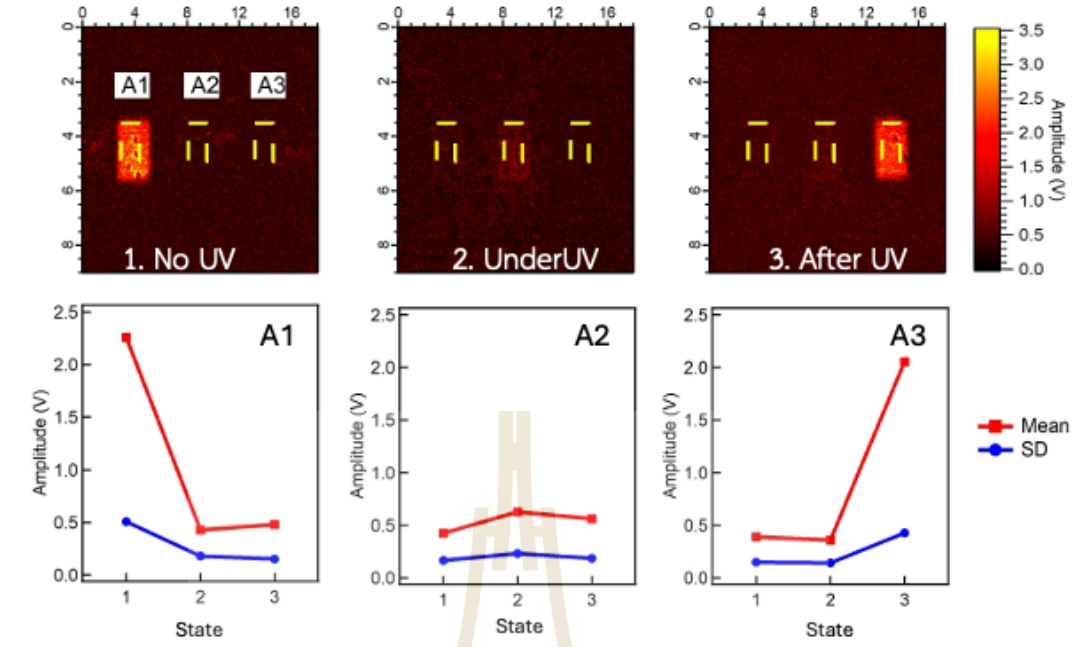

Figure 4.11 PFM amplitude measurements of BFO film on NSTO under different UV states (poling -10V) : No UV (State 1), Under UV (State 2), and After UV (State 3). The top row displays the PFM amplitude images for each state, while the bottom row shows the mean and standard deviation (SD) of the amplitude for three areas (A1, A2, and A3) across the different states.

In contrast, the effect of UV irradiation on the sample with -10V applied voltage is drastically different from the -10V condition discussed earlier. The amplitude between states ($A_{1,1}$) and ($A_{1,2}$) remains mostly the same, indicating that UV exposure no longer reduces the ferroelectric response. However, there is a significant decrease over time from state ($A_{1,2}$) to ($A_{1,3}$). Additionally, there is a notable difference between ($A_{2,2}$) for both -10V and +10V applied voltage states. For the +10V condition, a significant increase in amplitude is observed, whereas only a slight increase is found for the -10V condition. Similar to the trend observed between states ($A_{1,2}$) and ($A_{1,3}$), the decay over time from state ($A_{2,2}$) to ($A_{2,3}$) is also pronounced. Interestingly, in area A3, we found that the amplitude increases under UV irradiation even without applied voltage, from state ($A_{3,1}$) to ($A_{3,2}$). However, the poling process after UV irradiation

seems to be ineffective, as the amplitude remains mostly the same from state ($A_{3,2}$) to state ($A_{3,3}$).

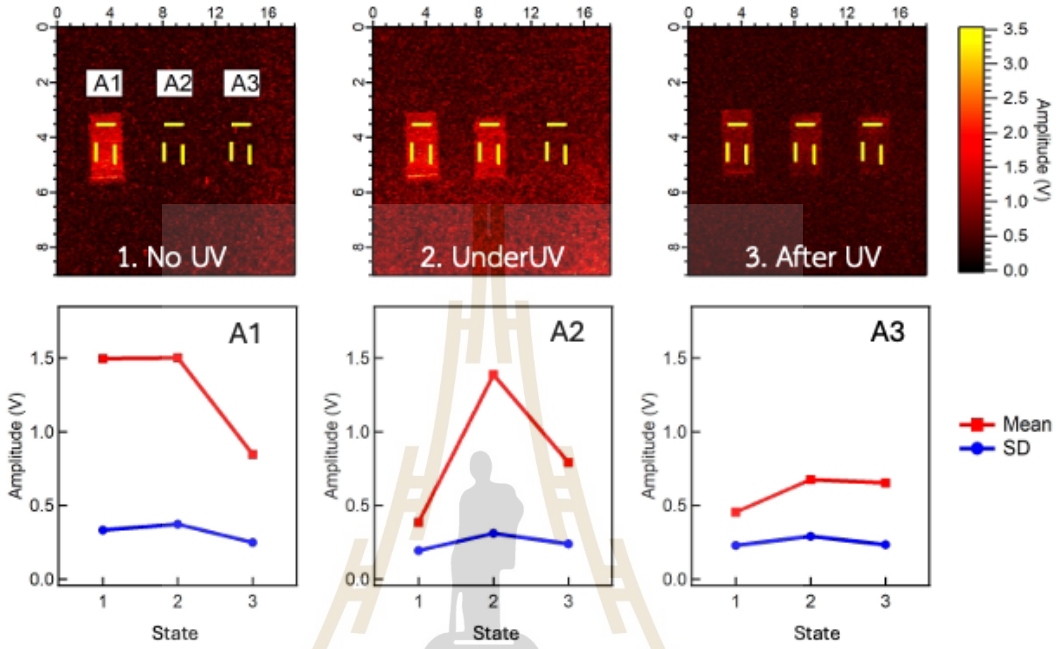

Figure 4.12 PFM amplitude measurements after +10V poling of BFO film on NSTO under different UV states: No UV (State 1), Under UV (State 2), and After UV (State 3). The top row displays the PFM amplitude images for each state, while the bottom row shows the mean and standard deviation (SD) of the amplitude for three areas (A1, A2, and A3) across the different states.

From earlier, we showed that UV exposure significantly reduces ferroelectric response due to photo-induced charge carriers, with partial recovery after UV removal. Differences in -10V and +10V poling conditions highlighted the role of the electric field in these changes. To deepen our understanding, we aim to investigate how varying UV exposure times affect the ferroelectric properties. The BFO/NSTO sample was also investigated using the PFM amplitude and phase over time under two conditions: No UV and Under UV. The poling voltage applied is -10V and +10V. The measurements were taken at intervals of 1, 2, 4, 6, 8, and 10 minutes under no UV

and UV on. The graphs display the mean (red line) and standard deviation (SD) in blue line of the amplitude and phase over time as illustrated in Figure 4.13.

For the -10V poling with No UV condition in the Figure 4.13(a) and Figure 4.14(c), the amplitude decreases steadily over time and shows a clear decline from the initial measurement, indicating a fading ferroelectric response. While the SD remains relatively low and stable. The phase remains stable over time, with minimal changes in both mean and SD values. This indicates that the polarization direction is maintained, despite the reduction in amplitude. However, the amplitude under UV condition in Figure 4.13(b) decreases rapidly within the first minute of UV exposure and continues to decline over time, but at a slower rate than the initial drop. This indicates that UV exposure accelerates the reduction in ferroelectric response. The SD remains low, like the No UV condition. In addition, the phase in Figure 4.13(d) shows slight changes and is less stable compared to the No UV condition, remaining relatively stable over time. The SD increases somewhat, indicating more variability in the phase under UV exposure.

For the +10V poling with No UV condition in the Figure 4.13(e) and 4.13(g), the amplitude drops significantly after the first minute and then it slightly increases from 2 minutes to 6 minutes. Additionally, it starts reducing again for the last 4 minutes with a small magnitude. The phase significantly increases in the first minute, then gradually reduces from 2 minutes to 8 minutes. The increasing of phase shows again at 10 minutes. In the case of UV exposure, the amplitude drops at the 1-minute mark of UV exposure, then increases at 2, 4, and 6 minutes, and drops again after 8 and 10 minutes as demonstrated in Figure 4.13(f) and 4.13(h). This pattern is very similar to the without UV exposure case; however, the magnitude is much stronger. This fluctuation indicates that UV exposure induces more dynamic changes in the amplitude compared to the No UV condition. The SD remains low, like the No UV condition. The phase trend is also like the without UV condition, showing initial

instability. Then, it positively changes after 8 minutes of UV exposure. The SD increases somewhat, indicating more variability in the phase under UV exposure.

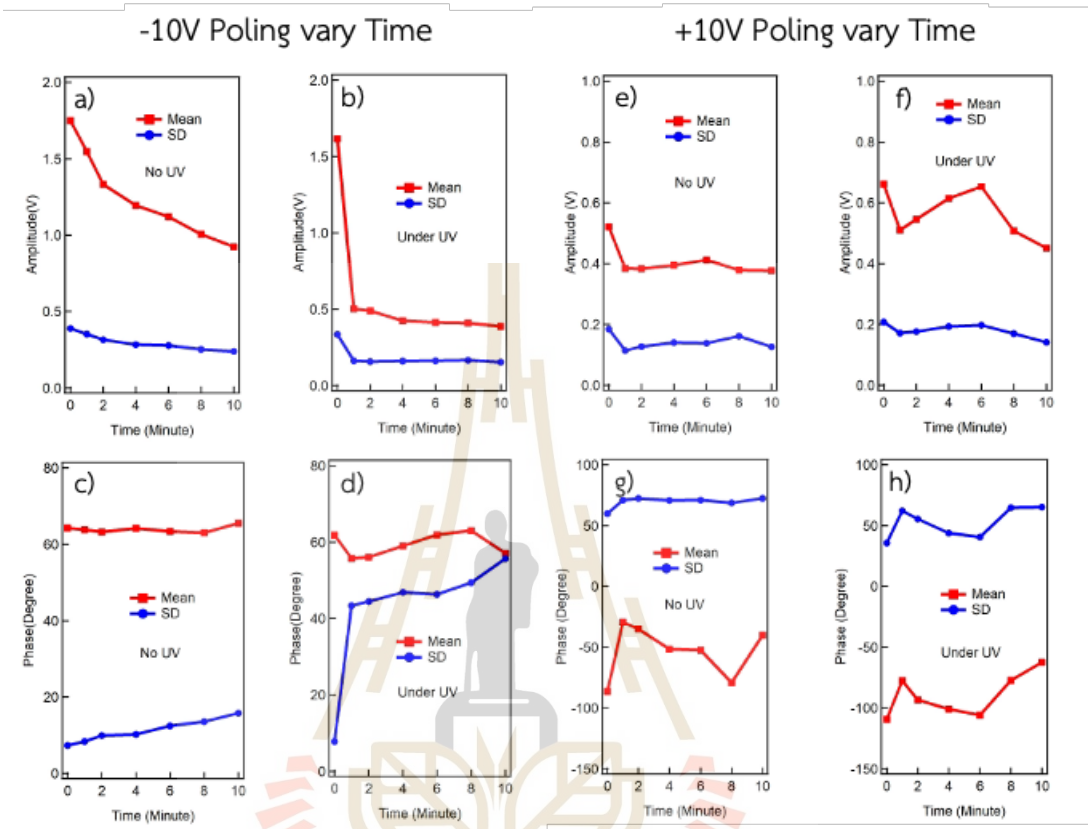

Figure 4.13 PFM amplitude and phase measurements of BFO/NSTO annealed over time with +10V and -10V poling under No UV and Under UV conditions.

From our result, we can suggest that both -10V and +10V poling conditions show a reduction in amplitude over time, especially under UV exposure. Notably, the reducing fashion of amplitude is similar between without UV and under UV irradiation with weak and strong magnitude, respectively. For -10V poling, the amplitude decreases steadily under No UV (decrease to 47%) and rapidly under UV (decrease to 76%). Moreover, the amplitude shows a significant decline under UV within the first minute and then stabilizes, indicating a fast initial response to UV exposure. For -10V poling, the amplitude drops significantly after the first minute under

No UV (down to 27.6 %) and then fluctuates with small margin. Under UV, the amplitude shows more dynamic changes (down to 31.7%), with strong fluctuations at different time points. The phase remains relatively stable in both conditions, with some fluctuations under UV exposure. For -10 V poling condition, the phase remains stable under No UV but shows slight variability under UV. While, for +10 V poling condition, the phase alternates between positive and negative values more prominently under No UV and stabilizes towards the end, while under UV, it shows greater variability and shifts to positive degrees at later times.

4.3 Polarization-Electric field Hysteresis Loop (P-E loop)

This study examines the ferroelectric properties of a BFO film (approximately 80 nm thick) on an NSTO substrate after annealing, using a P-E hysteresis loop to plot polarization (P) against the electric field (E). The graph presents three conditions: “No UV”, “Under UV”, and “After UV”. The gold top electrode size was 100 x 100 μm, and the bottom electrode was silver paste. The maximum voltage applied was ±1 V, corresponding to an electric field of ±200 kV/cm. The polarization of the samples was measured at 50 Hz, as shown in Figure 4.14. The P-E hysteresis loop under no UV exposure is oval-shaped, indicating both ferroelectric and resistive behavior. The remnant polarization (P_r), which is the polarization value at zero electric field, is 20.29 μC/cm² highest in this condition, showing strong ferroelectric properties. The coercive field (E_c), where the polarization switches direction, is 105.75 kV/cm, also highest in this condition. Under UV exposure, the P-E loop shows a shift from resistive to slightly ferroelectric behavior. Both the remnant polarization (4.81 μC/cm²) and coercive field (13.58 kV/cm) are reduced compared to the no UV condition. This reduction suggests that UV exposure introduces photo-induced charge carriers, affecting the material's ability to switch polarization and resulting in weaker ferroelectric properties. After UV exposure, the P-E loop shows partial recovery of the remnant polarization (17.45 μC/cm²) and coercive field values (79.35 kV/cm) compared to the Under UV

condition. This indicates that while some effects of UV exposure persist, the ferroelectric properties begin to revert to their original state once UV exposure stops. These findings highlight the influence of UV light on the ferroelectric behavior of BFO films and suggest potential for tunable ferroelectric properties through controlled UV exposure. This understanding is crucial for applications in optoelectronic devices and non-volatile memory where controlled switching of polarization states is required.

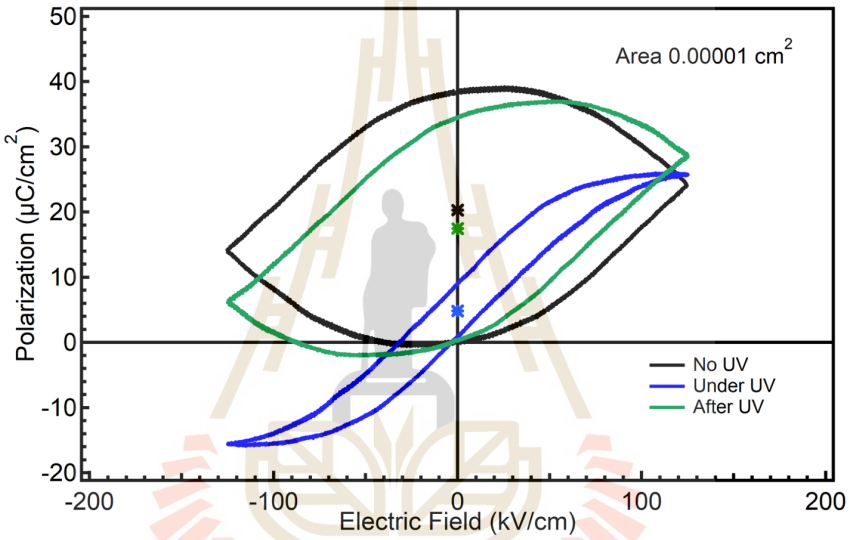

Figure 4.14 The P-E hysteresis loops of BFO/NSTO annealed under different conditions: No UV (black line), Under UV (blue line), and After UV (green line). The graph plots polarization (μC/cm²) versus electric field (kV/cm).

4.4 Voltage Response of Annealed BFO Film on NSTO Under Different UV Power Conditions

The voltage was measured between the top electrode and the bottom electrode with two conditions under UV exposure or without UV exposure. The results showed that the voltage remains relatively stable and close to 0 mV for all power levels when the UV is turned off. This indicates that without UV exposure, there is minimal photo-induced activity affecting the BFO film's voltage. On the other hand, the voltage rise is more significant at higher UV power levels, except for 0.3 mW which presents no response of the voltage. For the power of 14 mW (blue line), the voltage increases more noticeably, reaching approximately 0.7 mV. While the voltage can reach 2.4 mV when the power is 25 mW. This behavior indicates that higher UV power results in a greater photo-induced voltage response in the BFO film. When the UV is turned off again, the voltage decreases back to nearly 0 mV for all power levels. This decrease shows that the photo-induced effects are reversible and that the BFO film returns to its initial state when UV exposure is removed. The consistent increase in voltage when sample is under UV irradiation and the decrease without UV across all power levels confirm that UV exposure induces a reversible photo-voltaic effect in the BFO film. The effect is more pronounced with higher UV power.

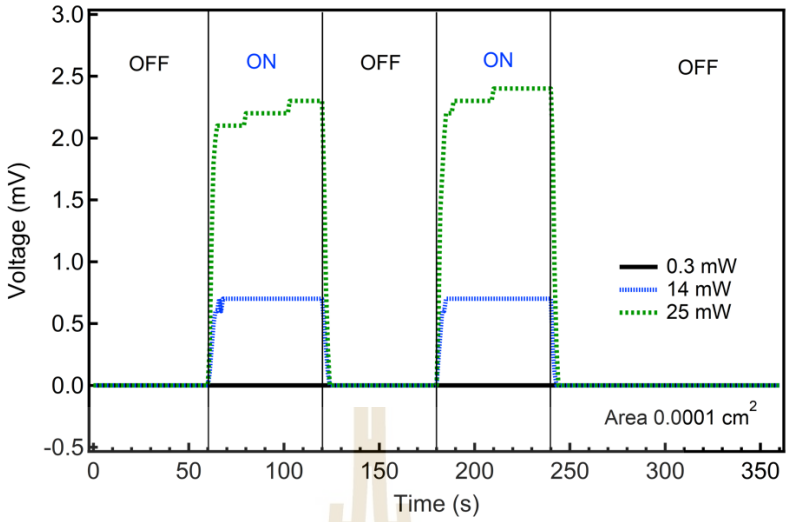

Figure 4.15 Voltage response over time for annealed BFO film on NSTO under different UV power conditions. The voltage was measured between the top and bottom electrodes. The graph shows the voltage response for UV power levels of 0.3 mW (black line), 14 mW (blue line), and 25 mW (green line). The voltage increases with UV ON and decreases with UV OFF, with higher UV power resulting in a greater photo-induced voltage response.

CHAPTER V
CONCLUSION AND FUTURE RESEARCH

5.1 Conclusions

For basic characterization, BFO thin films on various substrates were analyzed by using XRD, SEM, and EDS. The results demonstrated the effectiveness of the preparation and annealing processes in forming crystalline BFO thin films on NSTO and FTO substrates. XRD confirmed successful crystallization, while SEM provided detailed insights into surface morphology, showing improved crystallinity after annealing. EDS confirmed the elemental composition and successful deposition of the BFO layer.

The ferroelectric property of the BFO/NSTO annealed was confirmed by PFM to test the control of ferroelectricity on an unpatterned BFO/NSTO sample by creating small-sized letters. These results demonstrate that the sample, prepared by a simple method, can effectively show polarization by applying different voltages. The ability to create polarized letters down to 493 nm on the surface highlights the potential for data storage and nano-electronic devices. This study shows that the electric fields can change local polarization states, making it useful for studying small-scale domain changes and developing advanced technologies.

To the ferroelectric properties on different substrates and size effects, focusing on unpatterned samples, samples patterned by FIB, and samples with gold nanohole arrays patterned by EBL. The analysis of ferroelectric properties used topography, PFM amplitude and phase, and hysteresis loops to compare the effects of sample size and patterning. The study shows that the ferroelectric properties of BFO thin films are significantly affected by the size and patterning of the samples. There are two main pieces of evidence that nano-patterning affects ferroelectric properties. First, the domain switching capability varies from clear switching in the unpatterned area, to roughly switching in the nano-grid patterned by FIB, to rarely switching in the nanohole array by EBL.

Second, in terms of hysteresis loops, all three conditions exhibit typical ferroelectric behavior with different ferroelectric coefficients. Although the patterned conditions display smaller overall piezoresponse characteristics, their amplitude responses are more consistent compared to the unpatterned condition. These findings are important for applications in memory devices and sensors, where precise control of polarization is essential. In addition, the one experiment that was most interesting in our thesis was the effect of UV irradiation on ferroelectricity.

The PFM amplitude measurements indicate that UV exposure affects the ferroelectric response of BFO films under both +10V and -10V poling conditions. UV exposure reduces the polarization amplitude, and while partial recovery is observed after UV removal, the ferroelectric properties do not fully return to their initial state. The differences in response between +10V and -10V poling suggest that the direction of the electric field during poling may influence the extent of UV-induced changes. To deepen our understanding reducing of ferroelectric response due to photo-induced charge carriers, the PFM amplitude and phase measurements over time were investigated. The results reveal that UV exposure significantly impacts the ferroelectric properties of BFO films under both +10V and -10V poling conditions. UV exposure accelerates the reduction in amplitude and introduces greater variability in the phase.

The differences in response between +10V and -10V poling suggest that the direction of the electric field during poling influences the extent of UV-induced changes. Understanding these effects is crucial for developing optoelectronic devices that rely on stable ferroelectric properties and controlled by UV exposure. Moreover, the ferroelectric properties of an annealed BFO/NSTO were investigated by using P-E hysteresis loops and voltage response measurements under different UV power conditions. This study shows that UV exposure significantly affects the polarization, piezoresponse, and voltage dynamics of BFO/NSTO samples. The findings highlight the role of electron-hole pairs generated by UV light in screening internal electric fields, leading to decreased polarization and altered voltage behavior. These results are

crucial for understanding the behavior of ferroelectric materials under light exposure and have implications for their use in optoelectronic devices.

5.2 Improvement and future research

Perform annealing after patterning to repair damage from the patterning process. This could help recover ferroelectric properties by promoting re-crystallization and reducing defects. BFO films before patterning could apply protective coatings to shield the ferroelectric material from direct exposure to ion or electron beams. This can help keep the ferroelectric domains intact. Investigating the effects of other substrates and deposition methods could further understand the material's behavior and potential applications.

The decrease in polarization after UV exposure shows that photo-induced charge carriers affect ferroelectric properties. We must do more experiments in different samples condition such as unannealed, annealed with different temperature and compare with the STO substrate.